

ALICE-PUBLIC-2024-003
18 September 2024

Supplemental figures:
**Measurement of the inclusive isolated-photon production cross section in
pp and Pb–Pb collisions at $\sqrt{s_{NN}} = 5.02$ TeV**

ALICE Collaboration*

Abstract

The following note presents supplemental figures and additional material for the paper: “Measurement of the inclusive isolated-photon production cross section in pp and Pb–Pb collisions at $\sqrt{s_{NN}} = 5.02$ TeV” [1]. A description of the calorimeter cell clusterization algorithm and cell selection for the shower spread calculation is presented. Supplementary figures are provided: shower shape distributions, including the effect on the variation of the cross-talk emulation parameters in the simulation; the underlying event subtraction with different area definitions; and isolated photon efficiency. Systematic uncertainty summary tables and figures are presented. The purity calculation method is described. The shower shape and isolation momentum correlation effect on the purity calculation is discussed. Purity fit values are provided. Dedicated cross section, ratio data-to-theory, and $R = 0.2$ over $R = 0.4$ ratio plots for the Pb–Pb collisions centrality class 50–90% are presented. A comparison to the Z^0 boson results from CMS is shown. Finally, the ratio of cross sections in Pb–Pb collisions central to semi-central or semi-peripheral is also included.

© 2024 CERN for the benefit of the ALICE Collaboration.

Reproduction of this article or parts of it is allowed as specified in the CC-BY-4.0 license.

*See Appendix A for the list of collaboration members

Contents

1	Clusterisation algorithm	3
2	Shower shape and cross-talk emulation	3
3	Particle isolation	5
3.1	Underlying event estimation with different areas	5
3.2	Isolated photon efficiency per selection criterum	8
3.3	Cumulative isolation fraction	8
4	Purity: The ABCD method	11
4.1	Method	11
4.2	Shower shape–isolation momentum correlation: Shower shape double ratios of isolated to anti-isolated and data over simulation	13
4.3	Sigmoid fits	15
5	Systematic uncertainties	17
5.1	Purity, cross section, and normalisation	17
5.2	pp collisions cross sections ratio at different centre-of-momentum energies	23
5.3	Ratio of yields with different cone radius	23
5.4	Nuclear modification factor	23
6	Results	26
6.1	Nuclear modification factor using pQCD NLO as pp collisions	26
6.2	Pb–Pb collisions 50–90% centrality class	27
6.3	Nuclear modification factor in ALICE and CMS	30
6.4	Comparison of the isolated photon and Z boson cross section and nuclear modification factor as a function of the centrality class: Check of the binary scaling factor	31
6.5	Ratio of isolated-photon cross sections in Pb–Pb collisions: central to semi-central or semi-peripheral	32
A	The ALICE Collaboration	37

1 Clusterisation algorithm

Particles deposit their energy in several calorimeter cells, forming a cluster. Clusters are obtained by grouping all cells whose energy is above 100 MeV and share common sides, starting from a seed cell, which has an energy deposit of at least 500 MeV. Because of the large particle multiplicity and contribution of the underlying event, contributions from several particles can easily be merged into the same cluster. This is especially important in central heavy-ion collisions. To avoid this, an additional condition has been applied with respect to previous measurements of isolated photons to restrict the growth of the cluster: cells are only added to the cluster if the cell energy decreases when moving away from the seed cell. Although this condition was targeted to Pb–Pb collisions, it has also been applied to the pp measurements presented here for consistency. Unfortunately, reconstructing the clusters this way also prevents the neutral meson decays into two photons from being merged into a single cluster and recognised as meson decays. This results in losing the ability to remove the clusters produced by meson-decay photons when the distance between shower edges is larger than a calorimeter cell size, i.e. when the energy is below 20 GeV for the π^0 , or below 40 GeV for the η . A way to circumvent this problem is presented in Sect. 3.2 of Ref. [1]: the cluster energy spread dispersion (shower shape, σ_{long}^2 [1, 2]) is calculated in a 5×5 window centred at the highest energy cell of the cluster. Figure 1 schematically shows the cell cluster selection in this measurement for the cluster energy and position (V2) and the shower shape calculation (5×5).

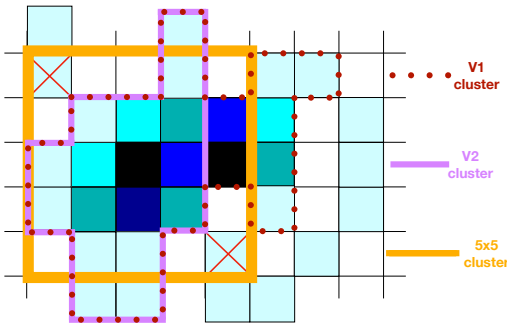


Fig. 1: (colour online) Schematic view of the cell energy repartition of two high-energy decay photons from a neutral meson, each centred in the black-filled cells, on top of a high-multiplicity low-energy particle underlying event, the lightest blue cells. The grey lines are the contour of cells selected restricting the growth of the cluster (V2) used here to calculate the cluster energy and position. The orange square is the 5×5 region around the highest-energy cell used for the shower shape calculation, excluding cells that only have a common corner, red crossed. The red dotted lines are the contour of a cluster without growth restriction (V1), as used in previous pp and p–Pb isolated photon analyses [3–5].

2 Shower shape and cross-talk emulation

Figure 2 shows the $\sigma_{\text{long}, 5 \times 5}^2$ distribution versus p_T for inclusive clusters in the five Pb–Pb collisions centrality bins and in pp collisions with the corresponding selection limits. Additional centrality classes are included here with respect the equivalent figure in Ref. [1]. One can appreciate the photon and π^0 bands in all the frames, even hints of the η band at high p_T .

The cross talk between cells modifies the shower shape distribution, widening the single-photon-cluster peak distribution to $\sigma_{\text{long}, 5 \times 5}^2$ values larger than 0.25, as discussed in detail in Ref. [2]. This effect was modelled in the simulation by adding, for a given cell, a small fraction of its energy E_{cell} into the surrounding cells with energy $E_{i,j}$ (column i , row j with respect to the reference cell) in the same T-Card. The induced energy is then $E_{i,j}^{\text{ind}} = F^{\text{ind}} E_{\text{cell}}$, with $F^{\text{ind}} = \mu_1 + \mu_2 E_{\text{cell}}$ where μ_1 and μ_2 depend on the supermodule. If F^{ind} is above or below a given value $F_{\text{max}}^{\text{ind}}$ or $F_{\text{min}}^{\text{ind}}$, respectively, those values are used instead. Each resulting $E_{i,j}^{\text{ind}}$ is smeared by a Gaussian random distribution with width σ_{ind} . Additionally, the amount of induced energy is limited for lower energies in order not to provoke additional cluster nonlinearity, by requiring: $E_{i,j} + E_{i,j}^{\text{ind}} > 100$ MeV, the same limit as the clusterisation minimum cell energy. Finally, the total induced energy after smearing in the nearby T-Card cells is subtracted from the

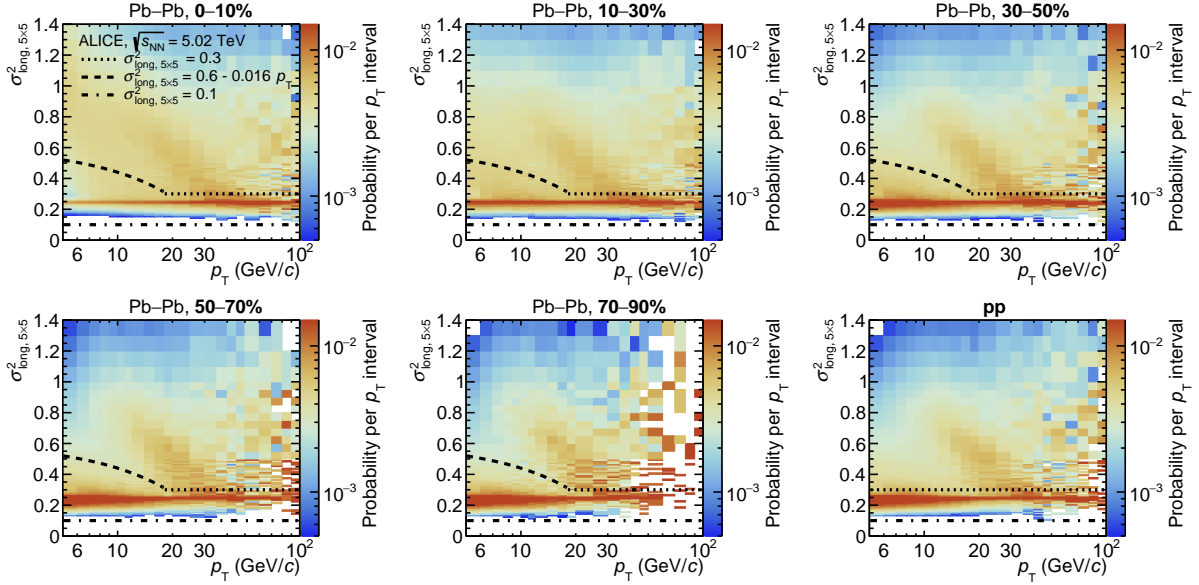


Fig. 2: (colour online) Inclusive-cluster $\sigma_{\text{long}, 5 \times 5}^2$ distribution (basic cluster selection plus track–cluster association rejection for Pb–Pb collisions) as a function of p_T in data for pp (lower right frame) and Pb–Pb collisions for five different centrality classes. The dotted line corresponds to the tight value of the upper selection limit for single photon candidate clusters (narrow clusters) and the dashed line corresponds to a looser photon upper selection used in Pb–Pb collisions below 18 GeV/c. The dotted-dashed line corresponds to the narrow cluster’s lower limit.

main signal cell, $E_{\text{cell}}^{\text{final}} = E_{\text{cell}} - \Sigma E_{i,j}^{\text{ind}}$, so that the energy scale is conserved. The cross-talk parametrisation obtained from pp collisions in Ref. [2] is found to induce a too-strong shape modification in Pb–Pb central collisions. Decreasing the $F_{\text{min}}^{\text{ind}}$ limit by a factor two with respect to [2] has been found to result in a better agreement between data and simulation for central as well as peripheral Pb–Pb collisions, without worsening the agreement in pp collisions. The final cross-talk emulation parameters used in the simulation are summarised in Table 1.

Table 1: Parameters used in the cross talk emulation in the simulation (see text), for the different groups of supermodules.

	group 1	group 2	group 3	group 4
SM number	3, 7	1, 10	0, 2, 4, 5, 6, 11	8, 9
	-	-	12, 13, 16	14, 15, 17, 18, 19
$F_{\text{min}}^{\text{ind}}$	0.3%	0.25%	0.235%	0.175%
$F_{\text{max}}^{\text{ind}}$	1.8%	1.6%	1.6%	1.6%
μ_1	1.2%	1.2%	1.15%	0.8%
μ_2 (GeV ⁻¹)	-0.11%	-0.11%	-0.11%	-0.11%
σ_{ind}	0.5%	0.5%	0.5%	0.5%

Figure 3 shows a projection of the inclusive-cluster $\sigma_{\text{long}, 5 \times 5}^2$ distribution from data in Fig. 2 and simulation (γ -jet plus jet–jet PYTHIA 8) for a low- and a high- p_T interval and for central Pb–Pb collisions and pp collisions: a reasonable description is achieved in simulation after including a modelling at the cell energy level of the electronics cross talk introduced in Sect. 2. This new modelling that is used for this measurement, is compared to the one used in previous ALICE measurements [3, 4, 6] and also compared without the modelling for the full simulation including signal and background or only signal. One can appreciate the better agreement of the new modelling and how the cross talk changes the shower shape distribution width from the ideal case without modelling.

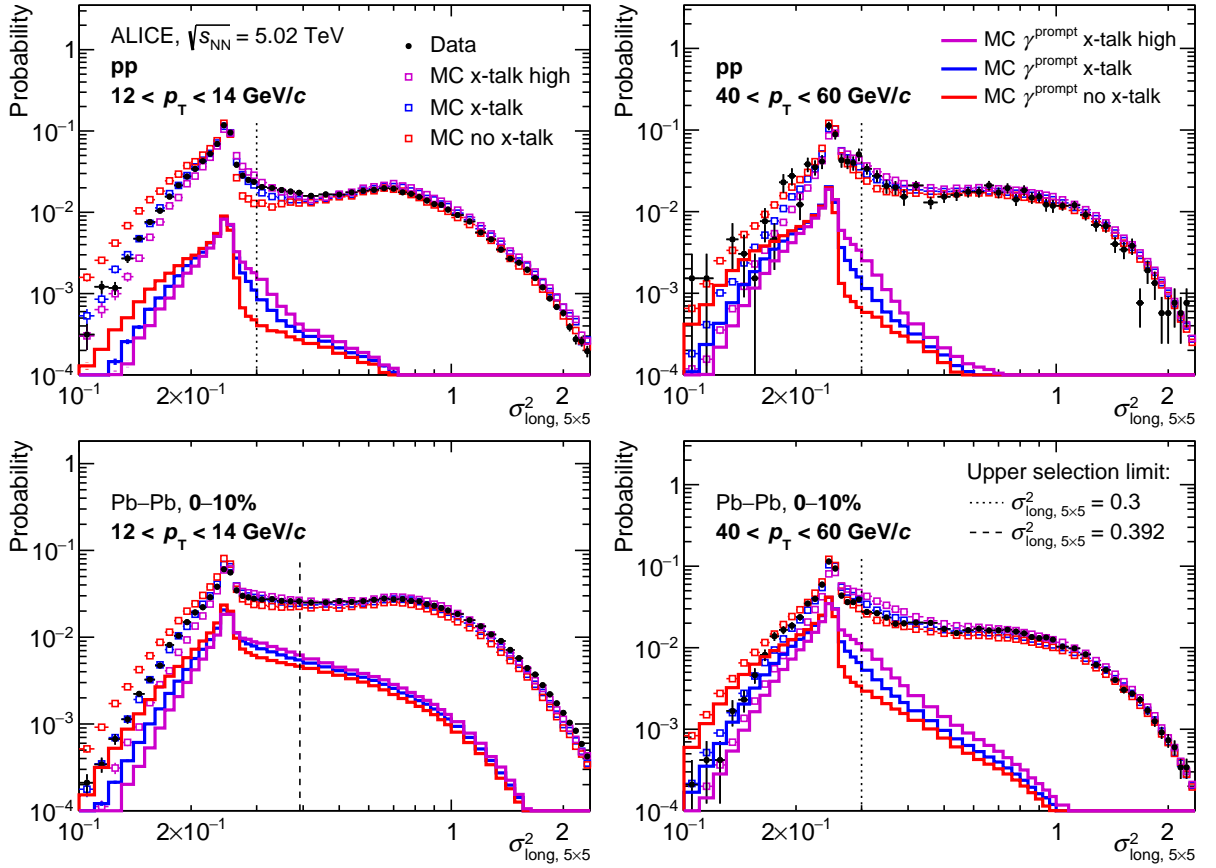


Fig. 3: (colour online) Inclusive-cluster $\sigma_{\text{long}, 5 \times 5}^2$ distribution in data (black bullets) and PYTHIA 8 simulation (jet–jet+ γ –jet processes). Three different treatments of cross talk (x-talk) considered in the simulation: “no x-talk” (open red squares); “x-talk high” (open magenta squares), stronger cross talk obtained for the previous isolated-photon measurements [2–4]; and “x-talk” (open blue squares), obtained for this measurement. The four panels display these distributions for two selected cluster p_T ranges, $12 < p_T < 14$ GeV/c on the left and $40 < p_T < 60$ GeV/c on the right, and two collision systems: pp (top) and Pb–Pb 0–10% central (bottom). The simulation is also shown for signal prompt γ (γ^{prompt}) for the different x-talk cases (lines with the same colour code as for the full simulation). The tight narrow cluster range maximum value $\sigma_{\text{long}, 5 \times 5}^2 = 0.3$ or 0.392 (corresponding to $\sigma_{\text{max}}^2(13 \text{ GeV}/c)$) is shown on all plots as a dotted or dashed vertical line, respectively.

3 Particle isolation

3.1 Underlying event estimation with different areas

The isolation momentum is the sum of the transverse momenta of all the charged tracks (ch) that fall into the cone, from which an estimation of the underlying event (UE) tracks entering the cone is subtracted

$$p_T^{\text{iso, ch}} = \sum p_T^{\text{track}} - \pi \times R^2 \times \rho_{\text{UE}}. \quad (1)$$

where ρ_{UE} is the UE track p_T density.

The ρ_{UE} is estimated event-by-event by summing the track p_T in a rectangular area called “ η -band” centred around the azimuth ϕ^γ of the candidate cluster. Its short side has a width $\Delta\phi = \phi^{\text{track}} - \phi^\gamma$ that depends on R while its long side covers the full track acceptance: $|\eta| < 0.9$. Other areas were also considered: a ϕ -band that covers the same η region as the isolation-cone radius but covers $\Delta\phi = \pi$, limited to avoid the jet emitted in the opposite direction with respect to the photon candidate; perpendicular bands that cover the same area as the ϕ -band but centred at $\phi = \pm\pi/2$ from the photon; cones perpen-

dicular to the isolated-photon candidate; and the FASTJET jet area/median package [7]. For the η -band and ϕ -band, an additional gap between the isolation cone and the UE estimation area is considered, $\Delta R_{\text{UE gap}} = 0.1$, to avoid jet remnants contribution as described in Ref. [1]. See a schematic description of all the areas and the gap in Fig. 3 of Ref. [1].

Figure 4 shows the $p_{\text{T}}^{\text{iso, ch}}$ distribution for the different studied UE estimators for narrow clusters, $0.1 < \sigma_{\text{long, } 5 \times 5}^2 < 0.3$, for PYTHIA 8 [8–10] simulations of γ -jet events embedded into minimum bias data. Figure 5 shows the distributions for wide clusters, $0.4 < \sigma_{\text{long, } 5 \times 5}^2 < 2$ for data and PYTHIA 8 simulations of jet–jet events embedded into Pb–Pb MB data, respectively.

The distributions obtained show that the various methods have similar performances, but the distributions for perpendicular cones and bands are wider, and the mean of the distribution of ϕ -band, jet-median and the perpendicular methods tends to be lower than zero for narrow clusters in the embedded signal simulation, unlike the η -band. All these methods are also more sensitive to the anisotropy in particle azimuthal distributions induced by the elliptic flow [11] in the area inspected, which could cause the observed differences. For this reason, they are not used as default.

Figure 6 shows the resulting $p_{\text{T}}^{\text{iso, ch}}$ distribution in data and embedded signal simulation after subtracting the UE estimated with the η -band for pp and Pb–Pb collisions in five centrality classes. This figure complements Fig. 5 of Ref. [1] by showing the distributions for all centrality classes.

The mean of the distributions for wide clusters in embedded jet–jet simulations (Fig. 5) tends to be larger than zero as expected due to the contribution of jet particles inside the cone since those clusters likely originate from a jet. In data, for narrow clusters (Fig. 6), the distributions are less shifted but the right tail of the distribution is higher also due to the contribution of jet particles, unlike in the γ -jet embedded simulation distributions (Fig. 4) which are symmetric with respect to the maximum of the distribution, as expected.

The width of the distribution is larger for $R = 0.4$ (lower panels) than for $R = 0.2$ (upper panels), due to the larger UE fluctuations in the isolation cone. For the same reason, the width decreases when moving to more peripheral collisions. The result of a Gaussian fit over the γ -jet simulation points using the η -band is reported in Table 2.

Table 2: Width of $p_{\text{T}}^{\text{iso, ch}}$ distributions shown in Fig. 6, estimated via the standard deviation σ of a Gaussian parametrisation to the data and PYTHIA 8 γ -jet simulation (embedded to MB data for Pb–Pb collisions), and for $R = 0.2$ and $R = 0.4$.

System	σ (GeV/c) for $R = 0.2$	σ (GeV/c) for $R = 0.4$
0–10% Pb–Pb	4.994 ± 0.004	12.278 ± 0.014
10–30% Pb–Pb	3.628 ± 0.003	9.015 ± 0.007
30–50% Pb–Pb	2.143 ± 0.001	5.466 ± 0.004
50–70% Pb–Pb	0.837 ± 0.002	2.569 ± 0.009
70–90% Pb–Pb	0.322 ± 0.001	1.005 ± 0.002
pp	0.1634 ± 0.0004	0.467 ± 0.002

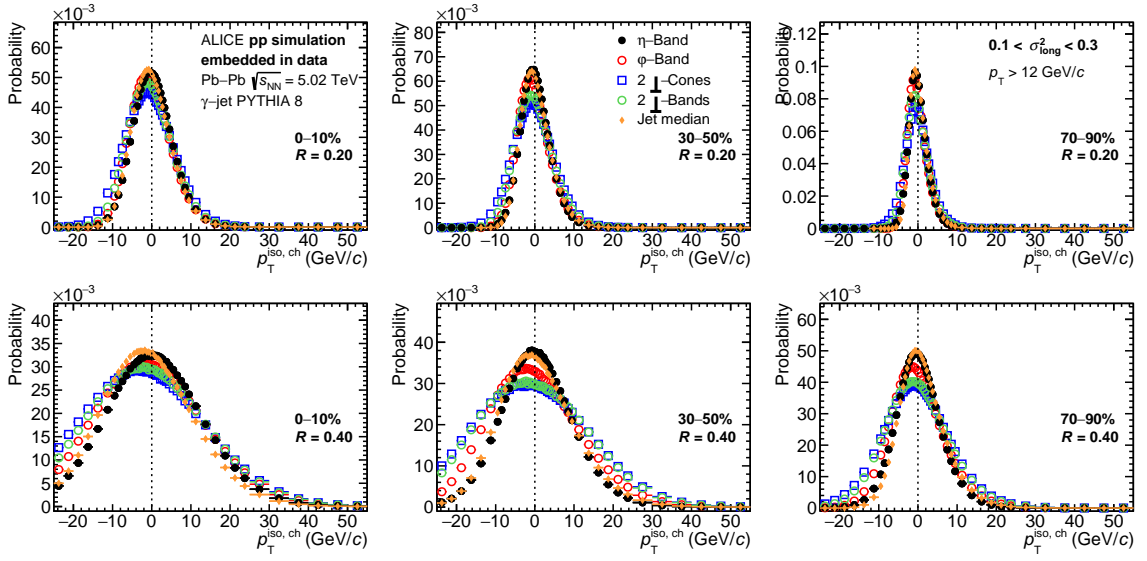


Fig. 4: (colour online) In γ -jet PYTHIA 8 simulation embedded into MB Pb–Pb data, $p_T^{\text{iso, ch}}$ distribution for different UE estimation areas described in the text, $p_T > 12$ GeV/c and narrow clusters with $0.1 < \sigma_{\text{long}, 5 \times 5}^2 < 0.3$ in Pb–Pb central (left), semi-central (middle) and peripheral (right) collisions for $R = 0.2$ (top) and $R = 0.4$ (bottom).

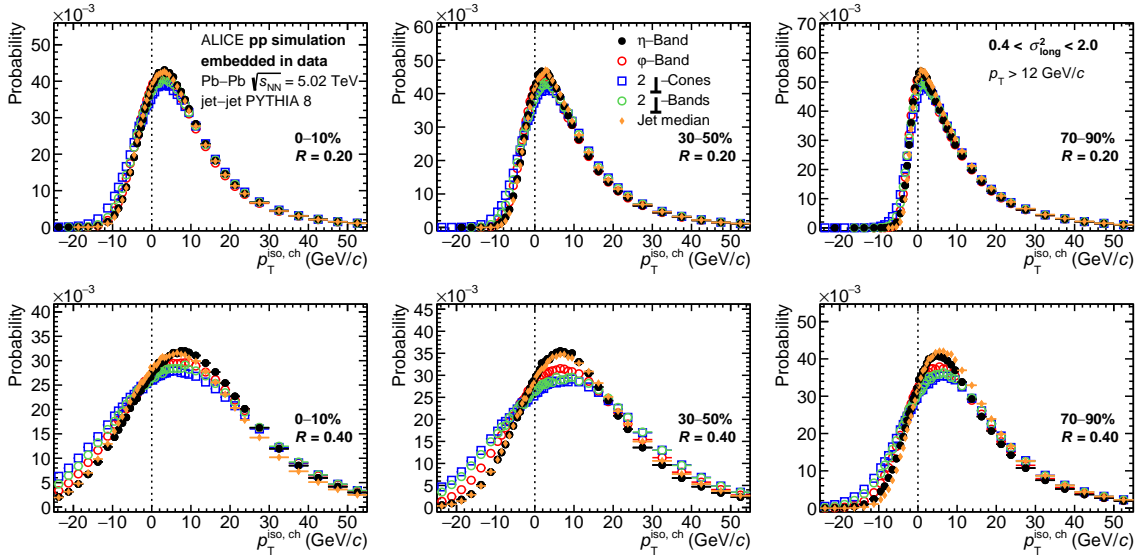


Fig. 5: (colour online) In jet-jet PYTHIA 8 simulation embedded into MB Pb–Pb data, $p_T^{\text{iso, ch}}$ distribution for different UE estimation areas described in the text, $p_T > 12$ GeV/c and wide clusters with $0.4 < \sigma_{\text{long}, 5 \times 5}^2 < 2$ in Pb–Pb central (left), semi-central (middle) and peripheral (right) collisions for $R = 0.2$ (top) and $R = 0.4$ (bottom).

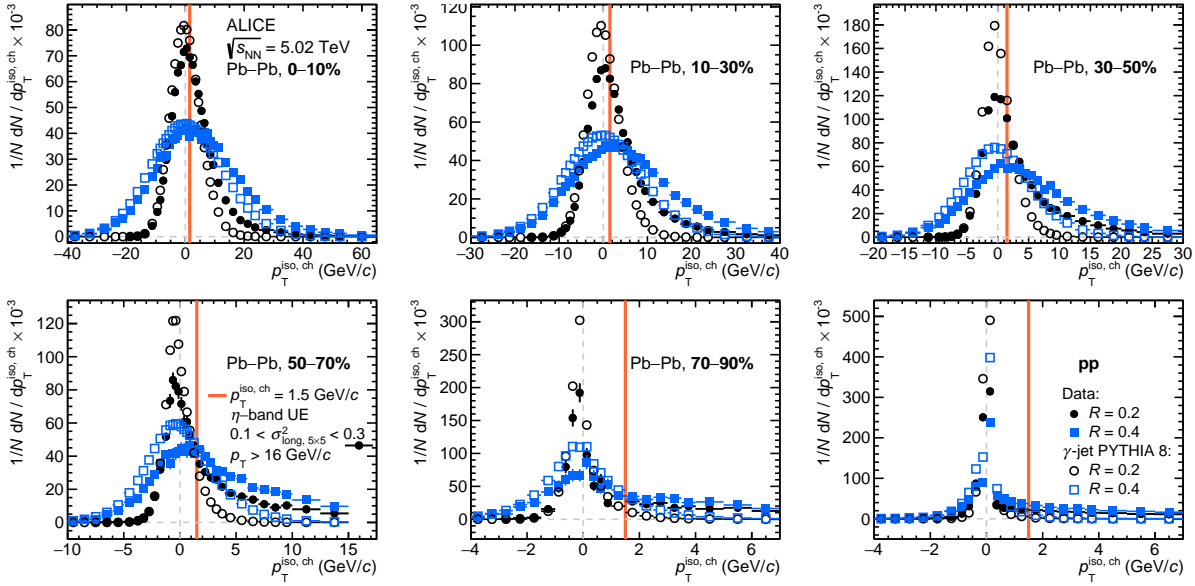


Fig. 6: (colour online) $p_T^{\text{iso, ch}}$ distribution for narrow clusters with $0.1 < \sigma_{\text{long, } 5 \times 5}^2 < 0.3$ for $p_T > 16$ GeV/c, in pp (lower right frame) and Pb–Pb collisions in five centrality classes, with $R = 0.2$ (black bullets) and $R = 0.4$ (blue squares), in data (full markers) and simulated PYTHIA 8 γ -jet processes (open markers), embedded into data in case of Pb–Pb collisions.

3.2 Isolated photon efficiency per selection criterum

The different analysis selection criteria determine the overall efficiency. Different efficiencies can be considered depending on the selection criteria: reconstruction ε^{rec} (inclusive clusters selection), photon identification ε^{id} (shower shape selection), and isolation ε^{iso} . They are calculated as the ratio of p_T^γ spectra, where the denominator is the number of generated photons $dN_\gamma^{\text{gen}}/dp_T^{\text{gen}}$, and the factors in the numerator are the reconstructed spectra after different selection criteria, $dN_{\text{cut}}^{\text{rec}}/dp_T^{\text{rec}}$. Figure 7 presents the different contributions as a function of p_T^γ for pp collisions and Pb–Pb collisions for all the centrality classes. This figure complements Fig. 7 of Ref. [1] where only two Pb–Pb centrality classes are shown, see the discussion on the efficiencies evolution with the selection criteria there. A smooth decrease of the different components of the efficiency can be appreciated from peripheral to central Pb–Pb collisions.

3.3 Cumulative isolation fraction

To decide the value of the isolation $p_T^{\text{iso, ch}}$ threshold, one can check how efficient the selection is on a known signal, γ -jet Monte Carlo simulation (MC) narrow clusters, and on background, data and jet–jet MC wide clusters. Figure 8 displays their selection cumulative probability for the two cone radii. The signal is largely accepted compared to the background in all systems if $p_T^{\text{iso, ch}}$ is selected smaller than a few GeV/c. However, there is a strong signal rejection in Pb–Pb collisions for the 0–10%, 10–30%, and 30–50% centrality classes. Comparing both cone radii, the discrimination power for the larger cone size ($R = 0.4$) is similar or a bit worse than that for $R = 0.2$ in central Pb–Pb collisions, but better in peripheral Pb–Pb and pp collisions at low $p_T^{\text{iso, ch}}$. The ratios of the distributions shown at the bottom of each panel, γ -jet simulation signal over the data or jet–jet simulation background, are rather constant until a certain $p_T^{\text{iso, ch}}$ value depending on the centrality: for central collisions to approximately 8 GeV/c and for peripheral Pb–Pb and pp collisions up to 2 to 3 GeV/c, above these values the ratio decreases. This indicates that the purity of the measurement will not significantly change below such values, while at higher p_T^γ the purity decreases. One can also observe that the distributions for wide clusters in data and background simulation do not match, this is due to the decay photon trigger in the jet–jet simulation.

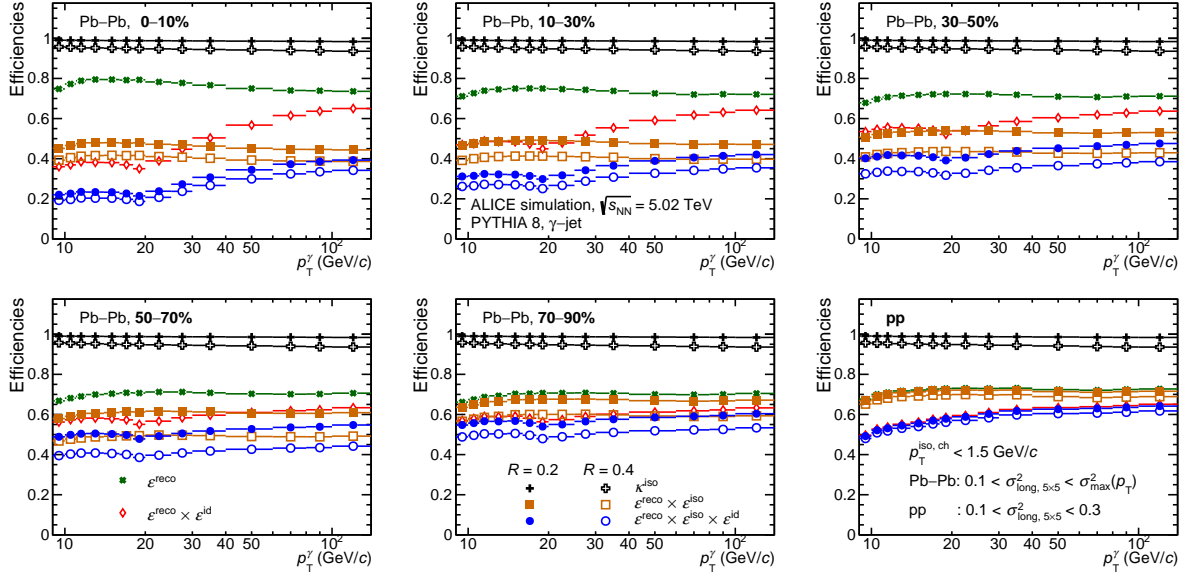


Fig. 7: (colour online) Contributions from reconstruction, identification, and isolation to the total efficiency calculated using Eq. 7 of Ref. [1], as a function of the reconstructed photon p_T^γ for pp (lower right frame) and Pb–Pb collisions for five centrality classes. Green markers: reconstruction efficiency ϵ^{rec} . Red or brown markers: efficiency additionally due to the photon identification by shower shape selection $\epsilon^{\text{rec}} \times \epsilon^{\text{id}}$ or the isolation criterion $\epsilon^{\text{rec}} \times \epsilon^{\text{iso}}$. Blue markers: efficiency due to the isolation criterion and shower shape selection $\epsilon^{\text{rec}} \times \epsilon^{\text{id}} \times \epsilon^{\text{iso}}$. Black markers: fraction κ^{iso} of generated photons which are isolated. Efficiency obtained from PYTHIA 8 simulations of γ -jet processes, embedded into Pb–Pb minimum bias data in the Pb–Pb case.

It can be concluded that using a tight $p_T^{\text{iso, ch}}$ selection value at $p_T^{\text{iso, ch}} < 1.5$ GeV/c like in previous pp and p–Pb analyses for all Pb–Pb centralities and in pp collisions is reasonable. A lower $p_T^{\text{iso, ch}}$ selection value would not provide much gain in background rejection power, would decrease the efficiency, and would complicate the comparison with theoretical predictions. Using a higher $p_T^{\text{iso, ch}}$ selection in central Pb–Pb collisions is possible, it would increase the efficiency of the measurement, but we prefer to use the same isolation selection criterion for all systems for simplicity.

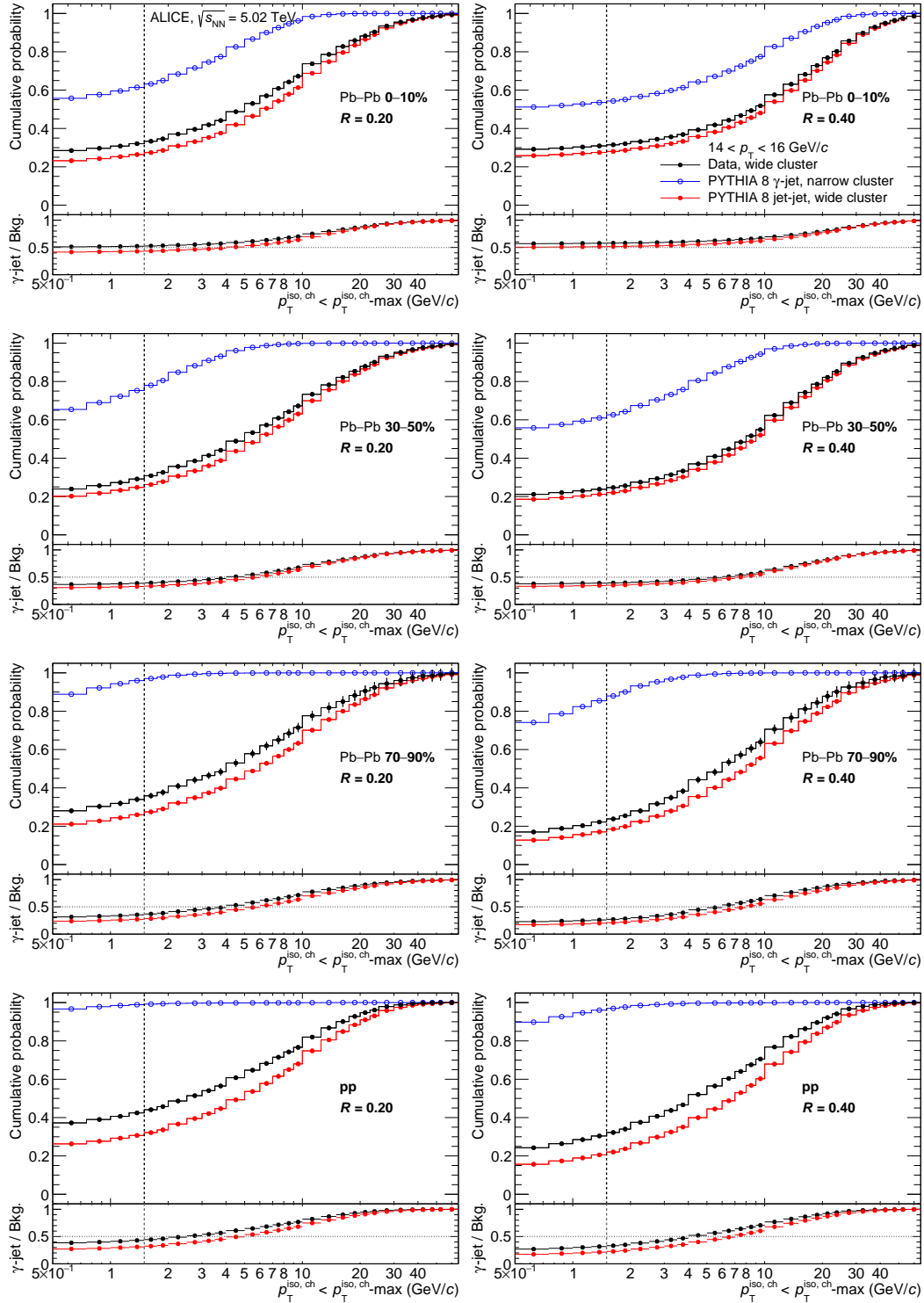


Fig. 8: (colour online) Fraction of inclusive clusters with $14 < p_T < 16$ GeV/c that pass the isolation selection as a function of the isolation momentum threshold for $R = 0.2$ (left) and $R = 0.4$ (right), for data wide clusters, signal γ -jet MC for narrow clusters and background jet-jet MC (with a photon with at least 3.5 GeV/c in the calorimeter acceptance) with for wide clusters. For Pb-Pb simulations, MC clusters are embedded into minimum bias Pb-Pb data. From top to bottom, 0–10% Pb-Pb collisions, 30–50% Pb-Pb collisions, 70–90% Pb-Pb collisions and pp collisions. Lower frame in each panel: ratio of the distribution for γ -jet MC clusters over the distributions for wide clusters in data and jet-jet MC. Horizontal dashed line set at $p_T^{\text{iso, ch}} = 1.5$ GeV/c.

4 Purity: The ABCD method

The isolated-photon candidate sample still contains a sizeable contribution from background clusters, mainly from neutral-meson decay photons. To estimate the background contamination, the same procedure as in Refs. [3, 4] is followed and presented here.

4.1 Method

Different classes of measured clusters were used: (1) classes based on the shower shape $\sigma_{\text{long}, 5 \times 5}^2$, i.e. *narrow* (photon-like) or *wide* (most often elongated, i.e. non-circular), and (2) classes defined by the isolation momentum $p_{\text{T}}^{\text{iso, ch}}$, i.e. *isolated* (iso) and *anti-isolated* ($\bar{\text{iso}}$). The different classes are denoted by sub- and superscripts, e.g. narrow isolated clusters are denoted $X_{\text{n}}^{\text{iso}}$, and wide anti-isolated clusters as $X_{\text{w}}^{\bar{\text{iso}}}$. The corresponding four classes **A**, **B**, **C** and **D** are represented schematically in Fig. 9 and on the measured distributions of $p_{\text{T}}^{\text{iso, ch}}$ versus $\sigma_{\text{long}, 5 \times 5}^2$ for two cone radii in Figs. 10 and 11.

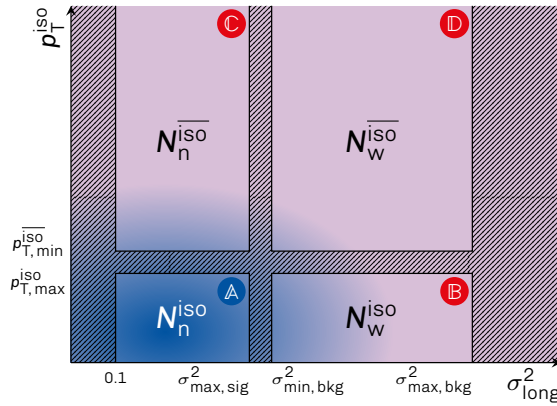


Fig. 9: (colour online) Illustration of the parametric space of the photon isolation momentum and the shower width parameter (σ_{long}^2), used to estimate the background yield in the signal class (**A**) from the observed yields in the three control classes (**B**, **C**, **D**). The red regions indicate areas dominated by the background and the blue regions are those that contain the photon signal. The colour gradient between these regions illustrates the presence of a signal contribution in the three background regions. See Figs. 10 and 11 for examples of this in data.

The $\sigma_{\text{long}, 5 \times 5}^2$ parameter values for narrow and wide clusters correspond to the signal and background clusters introduced in Sect. 3.2 of [1]. The wide clusters (mostly background) correspond to clusters with $0.4 < \sigma_{\text{long}, 5 \times 5}^2 < 2$ in pp collisions, and Pb–Pb collisions when $p_{\text{T}} < 18$ GeV/c. When $p_{\text{T}} > 18$ GeV/c in Pb–Pb, clusters are considered wide when $0.1 + \sigma_{\text{max}}^2 < \sigma_{\text{long}, 5 \times 5}^2 < 2$, with p_{T} dependent limit $\sigma_{\text{max}}^2(p_{\text{T}}) = 0.6 - 0.016 \times p_{\text{T}}$. The narrow clusters (containing most of the signal) are those with $0.1 < \sigma_{\text{long}, 5 \times 5}^2 < 0.3$ in pp collisions, and Pb–Pb collisions when $p_{\text{T}} < 18$ GeV/c. When $p_{\text{T}} \geq 18$ GeV/c in Pb–Pb, clusters are considered narrow when $0.1 < \sigma_{\text{long}, 5 \times 5}^2 < \sigma_{\text{max}}^2$. The anti-isolation criterion was set to $4 < p_{\text{T}}^{\text{iso, ch}} < 25$ GeV/c for all systems: the lower limit was placed far from the $p_{\text{T}}^{\text{iso, ch}} < 1.5$ GeV/c signal isolation momentum threshold, to have a gap available for systematic studies.

The yield of isolated-photon candidates in this nomenclature is $N_{\text{n}}^{\text{iso}}$. It consists of signal (S) and background (B) contributions: $N_{\text{n}}^{\text{iso}} = S_{\text{n}}^{\text{iso}} + B_{\text{n}}^{\text{iso}}$. The contamination of the candidate sample is then $C = B_{\text{n}}^{\text{iso}}/N_{\text{n}}^{\text{iso}}$, and the purity is $P \equiv 1 - C$. It is assumed that the ratios of isolated over anti-isolated background is the same in the narrow clusters range (**A** and **C**) and in the wide clusters range (**B** and **D**) so that

$$\frac{B_{\text{n}}^{\text{iso}}/B_{\text{n}}^{\bar{\text{iso}}}}{B_{\text{w}}^{\text{iso}}/B_{\text{w}}^{\bar{\text{iso}}}} = 1. \quad (2)$$

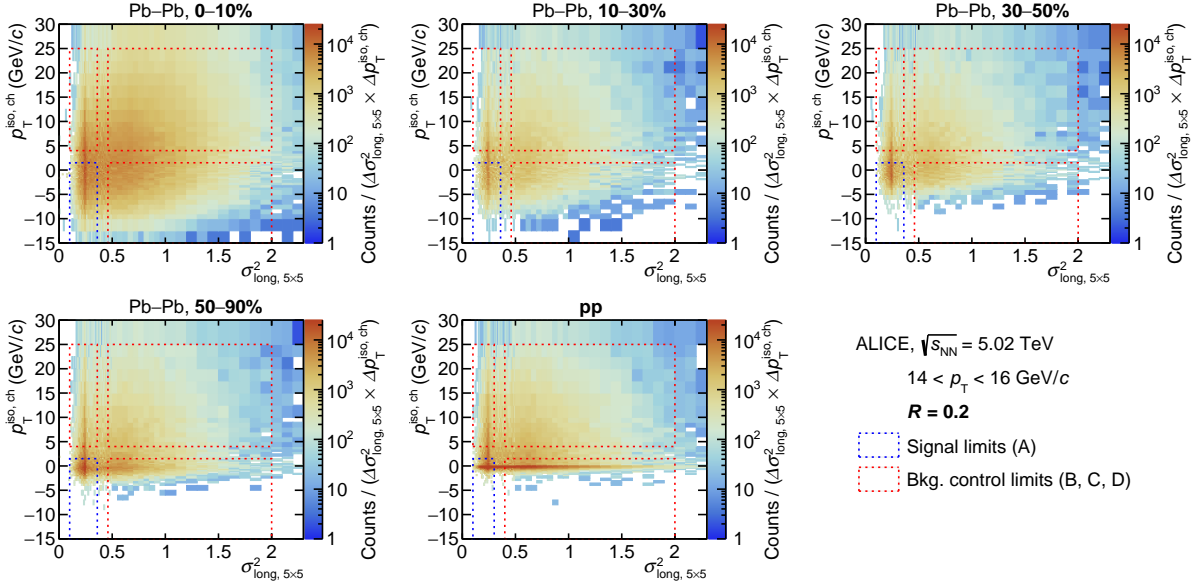


Fig. 10: (colour online) The parametric space of the cluster isolation momentum and the shower width parameter ($\sigma_{\text{long}, 5 \times 5}^2$) in data for $R = 0.2$ and $14 < p_T < 16$ GeV/c, used to estimate the background yield in the signal class (A) from the observed yields in the three control classes (B, C, D). The dashed boxes indicate the limits of each class, the lower signal $p_T^{\text{iso}, \text{ch}}$ selection is open.

Assuming that the amount of signal in the background-dominated cluster classes is negligible compared to the background, the purity can be derived in a data-driven approach (dd) as

$$P_{\text{dd}} = 1 - \frac{\overline{B_n^{\text{iso}}} / N_n^{\text{iso}}}{\overline{B_w^{\text{iso}}} / B_w^{\text{iso}}} = 1 - \frac{\overline{N_n^{\text{iso}}} / N_n^{\text{iso}}}{\overline{N_w^{\text{iso}}} / N_w^{\text{iso}}}. \quad (3)$$

Unfortunately, both assumptions are valid only approximately, especially Eq. (2). In PYTHIA 8 simulations with two jets imposed in the final state, meaning that there is only background in all of the four classes, an evaluation of Eq. (2) gives double-ratio values between 1 and 2 that strongly depend on p_T , on the collision system, on the centrality, as well as on the background $p_T^{\text{iso}, \text{ch}}$ range selected for the anti-isolation. Since these deviations from unity are considered to be due to particle kinematics and detector response, the simulation can be used to estimate this bias

$$\left(\frac{\overline{B_n^{\text{iso}}} / \overline{B_n^{\text{iso}}}}{\overline{B_w^{\text{iso}}} / \overline{B_w^{\text{iso}}}} \right)_{\text{data}} = \left(\frac{\overline{B_n^{\text{iso}}} / \overline{B_n^{\text{iso}}}}{\overline{B_w^{\text{iso}}} / \overline{B_w^{\text{iso}}}} \right)_{\text{MC}}. \quad (4)$$

This implies replacing Eq. (2) by the relation given in Eq. (4), which leads to the expression of the MC-corrected purity

$$P = 1 - \left(\frac{\overline{N_n^{\text{iso}}} / N_n^{\text{iso}}}{\overline{N_w^{\text{iso}}} / N_w^{\text{iso}}} \right)_{\text{data}} \times \left(\frac{\overline{B_n^{\text{iso}}} / \overline{N_n^{\text{iso}}}}{\overline{N_w^{\text{iso}}} / \overline{B_w^{\text{iso}}}} \right)_{\text{MC}} \equiv 1 - \left(\frac{\overline{N_n^{\text{iso}}} / N_n^{\text{iso}}}{\overline{N_w^{\text{iso}}} / N_w^{\text{iso}}} \right)_{\text{data}} \times \alpha_{\text{MC}} \quad (5)$$

where the MC contains the combination of jet-jet and γ -jet counts scaled to their respective cross sections.

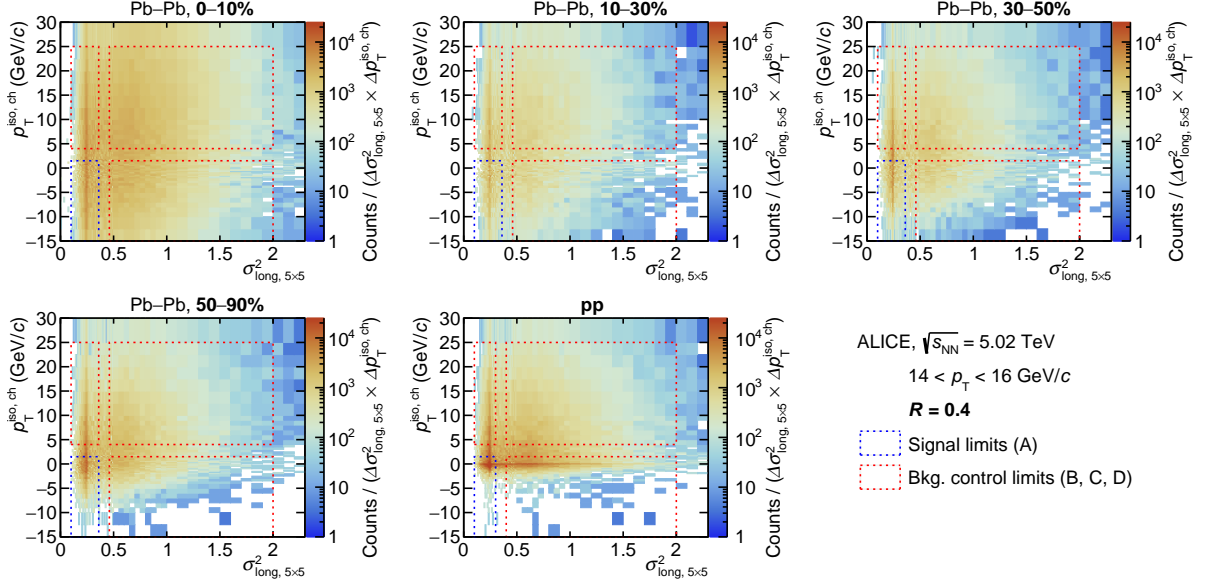


Fig. 11: (colour online) The parametric space of the cluster isolation momentum and the shower width parameter ($\sigma_{\text{long}, 5 \times 5}^2$) in data for $R = 0.4$ and $14 < p_T < 16$ GeV/c, used to estimate the background yield in the signal class (A) from the observed yields in the three control classes (B, C, D). The dashed boxes indicate the limits of each class, the lower signal $p_T^{\text{iso, ch}}$ selection is open.

4.2 Shower shape–isolation momentum correlation: Shower shape double ratios of isolated to anti-isolated and data over simulation

The difference between the degree of the correlation between isolation momentum and shower shape distribution in data and simulation is a potential source of bias, as it influences the validity of Eq. (4). To check this, the dependence of the double ratio

$$\frac{\left(N^{\text{iso}}/N^{\overline{\text{iso}}}\right)^{\text{data}}}{\left(N^{\text{iso}}/N^{\overline{\text{iso}}}\right)^{\text{MC}}} = f\left(\sigma_{\text{long}, 5 \times 5}^2\right) \quad (6)$$

on the shower shape width $\sigma_{\text{long}, 5 \times 5}^2$ is studied in a region where the signal contribution is expected to be negligible, i.e. large $\sigma_{\text{long}, 5 \times 5}^2$. If the correlation between the two variables is correctly reproduced in the simulation, the double ratio f should be independent of $\sigma_{\text{long}, 5 \times 5}^2$, and therefore, would be the same for wide and narrow background clusters. The double ratio was found to be above unity as shown in Figs. 12 and 13 for two p_T intervals, two isolation cone radii, and in the most extreme multiplicity cases, pp and central Pb–Pb, plus semi-central Pb–Pb to illustrate the evolution. The fact that the value of f exceeds unity indicates a larger isolation probability in data than in simulations. This is mainly due to an imperfect low p_T charged particle tracks MC performance and reconstruction effects leading to some discrepancy between data and simulation. Since the correction introduced by Eq. (5) relies on a narrow-over-wide clusters ratio, the overall normalisation in the double ratio of Eq. (6) is not relevant for this test. Note that the shift above unity in the figures is larger in pp collisions compared to Pb–Pb collisions because for the latter the simulation is embedded into real data and this reduces possible data versus simulation track performance effects.

However, in the large $\sigma_{\text{long}, 5 \times 5}^2$ region, $f(\sigma_{\text{long}, 5 \times 5}^2)$ has a slope. Since the slope is a sign of possible bias induced by differences between data and simulation, a correction was estimated by extrapolating to the small $\sigma_{\text{long}, 5 \times 5}^2$ region using a linear fit $p_0 + \sigma_{\text{long}, 5 \times 5}^2 \times p_1$ performed in the range above $\sigma_{\text{long}, 5 \times 5}^2 = 0.3$. This implies replacing the MC correction in Eq. (5) by a modified term

$$\alpha_{\text{MC}} \mapsto \alpha_{\text{MC}} \times \left(\frac{p_0 + \sigma_{\text{long}, \text{n}}^2 \times p_1}{p_0 + \sigma_{\text{long}, \text{w}}^2 \times p_1} \right), \quad (7)$$

where $\sigma_{\text{long}, \text{n}}^2$ and $\sigma_{\text{long}, \text{w}}^2$ are the median values of the inclusive-cluster $\sigma_{\text{long}, 5 \times 5}^2$ distribution in the narrow and wide ranges, respectively, and p_0 and p_1 are the parameters of the linear fit of the double ratio $f(\sigma_{\text{long}, 5 \times 5}^2)$. These extrapolations have then been used in the estimate of the uncertainties of the purity in Sect. 4 of Ref. [1]. This contribution is called isolation probability uncertainty source in Ref. [1]. The uncertainty is obtained by the difference between the α_{MC} factors obtained without and with the calibration according to Eq. (7), changing the $\sigma_{\text{long}, 5 \times 5}^2$ background region fit range: the average of the differences is used as uncertainty.

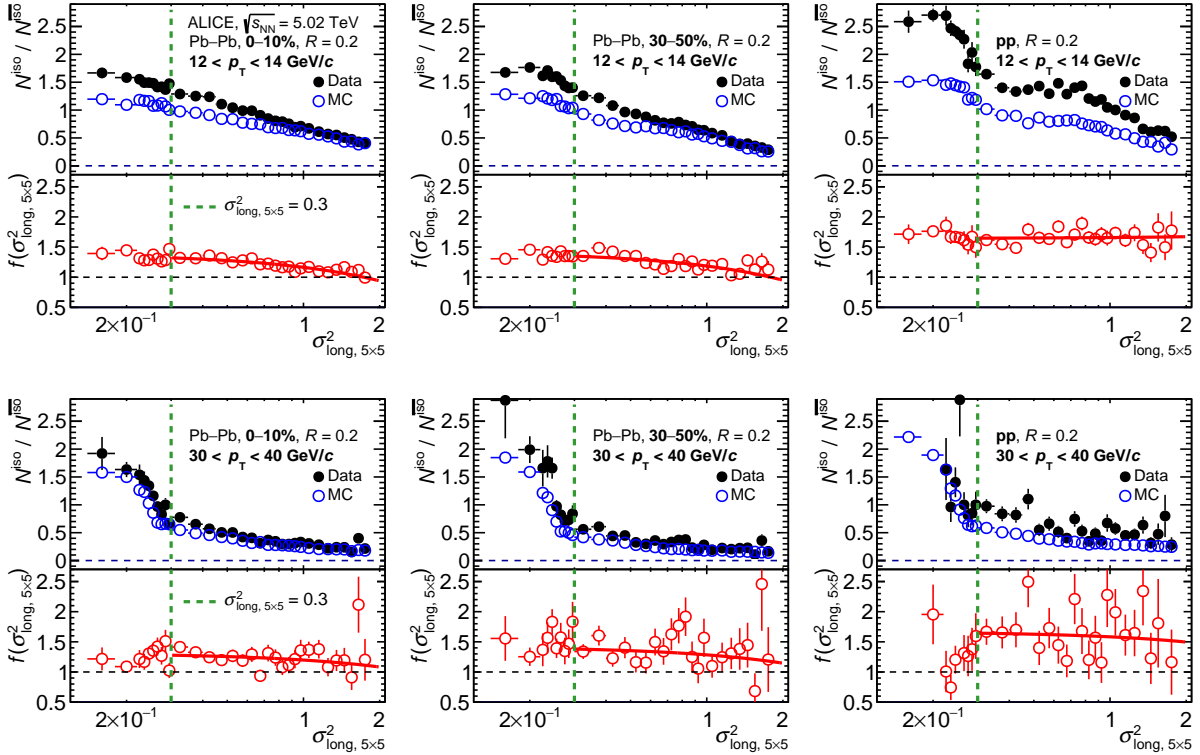


Fig. 12: (colour online) For each panel: Top, ratio of isolated and anti-isolated $\sigma_{\text{long}, 5 \times 5}^2$ distribution in data and simulation; Bottom, the ratio of the two, $f(\sigma_{\text{long}, 5 \times 5}^2)$. Top row for $12 < p_{\text{T}} < 14$ GeV/c and bottom row for $30 < p_{\text{T}} < 40$ GeV/c. Each row reports results for 0–10% (left) and 30–50% (middle) Pb–Pb collisions and pp collisions (right) for $R = 0.2$.

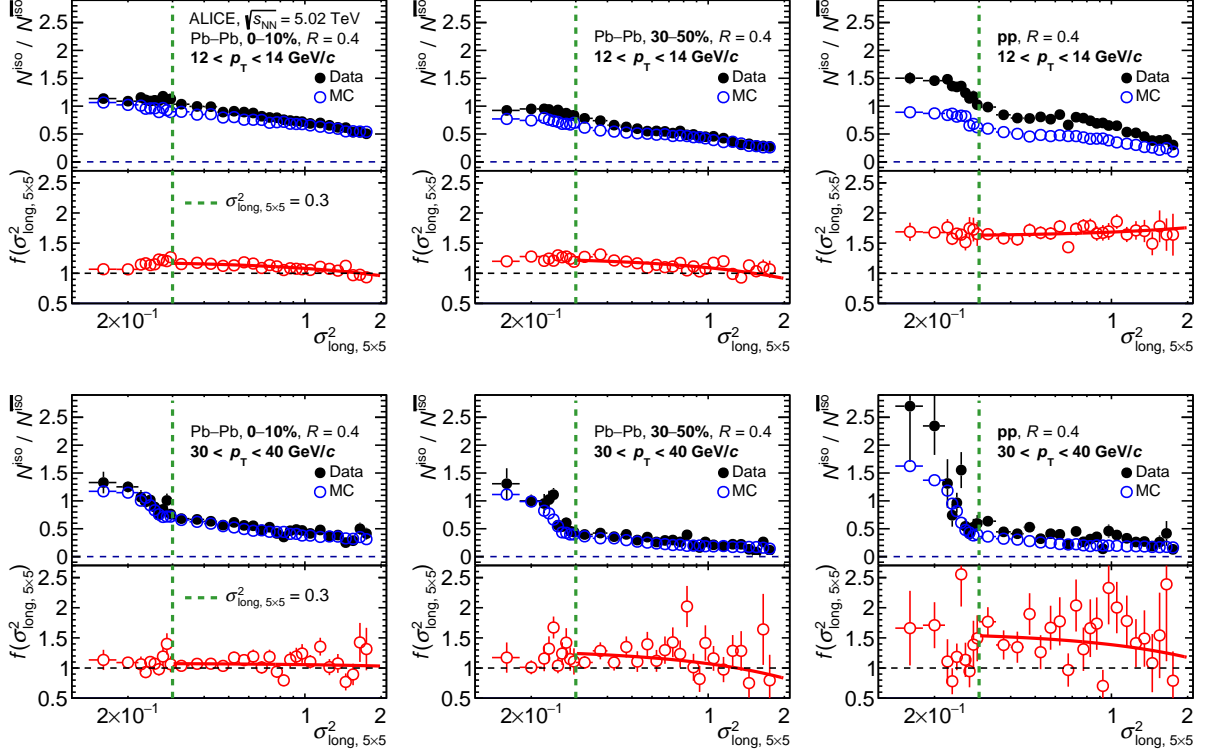


Fig. 13: (colour online) For each panel: Top, ratio of isolated and anti-isolated $\sigma_{\text{long}, 5 \times 5}^2$ distribution in data and simulation; Bottom, the ratio of the two, $f(\sigma_{\text{long}, 5 \times 5}^2)$. Top row for $12 < p_T < 14$ GeV/ c and bottom row for $30 < p_T < 40$ GeV/ c . Each row reports results for 0–10% (left) and 30–50% (middle) Pb–Pb collisions and pp collisions (right) for $R = 0.4$.

4.3 Sigmoid fits

To reduce the point-to-point statistical fluctuations in the purity used to correct the isolated-photon raw yield, the data points are fitted by two sigmoid functions to reproduce the shape of the distribution

$$f_i, \text{fit-sig}(p_T) = \frac{a_i}{1 + \exp(-b_i \times (p_T - c_i))}, \quad (8)$$

where i indicates two different fitting ranges, whose p_T limits depend on the collision system. The first fit is done from $p_T = 10$ – 14 to 40 – 60 GeV/ c and the second fit from $p_T = 20$ to 80 – 140 GeV/ c . This second fit is done only for the 0–10%, 10–30%, and 30–50% centrality classes of Pb–Pb collisions, where there are enough data points to reach above 60 GeV/ c and obtain a reliable fit. The outcome of the second fit is applied as purity correction only above 60 GeV/ c . In pp collisions, the fit is only done up to $p_T = 40$ GeV/ c , but the fit result is extrapolated to $p_T = 80$ GeV/ c since the last two p_T interval uncertainties are too large to obtain a reliable high- p_T fit. A slow rise with p_T can be expected in this range according to simulation studies and to the measurement in pp collisions at $\sqrt{s} = 13$ TeV, but the estimated size of the rise is covered by the uncertainties assigned.

The fit results are shown in Fig. 6 in Ref. [1]. The fit parameters are summarised in Table 3. The point uncertainties considered in the fit are the total uncertainties calculated as explained in Ref. [1]: The statistical and systematic uncertainty sources are added in quadrature to get an uncertainty σ_P ; Then, the points are moved and down by $1\sigma_P$, and fitted; The total uncertainty results from the average of the fits.

Table 3: Sigmoid function fit range and parameters for $R = 0.2$ and $R = 0.4$ from Fig. 6 in Ref. [1].

System	R	fit p_T range (GeV/ c)	a	b (c/GeV)	c (GeV/ c)
0–10% Pb–Pb	0.2	$10 < p_T < 60$	0.65	0.34	9.8
0–10% Pb–Pb	0.4	$10 < p_T < 60$	0.60	0.33	10.2
0–10% Pb–Pb	0.2	$20 < p_T < 140$	1.0	0.006	-78
0–10% Pb–Pb	0.4	$20 < p_T < 140$	0.81	0.007	-106
10–30% Pb–Pb	0.2	$10 < p_T < 60$	0.62	0.35	10.6
10–30% Pb–Pb	0.4	$10 < p_T < 60$	0.56	0.30	10.4
10–30% Pb–Pb	0.2	$20 < p_T < 140$	1.0	0.011	-14.5
10–30% Pb–Pb	0.4	$20 < p_T < 140$	1.0	0.010	12.4
30–50% Pb–Pb	0.2	$10 < p_T < 60$	0.61	0.25	11.0
30–50% Pb–Pb	0.4	$10 < p_T < 60$	0.54	0.29	11.1
30–50% Pb–Pb	0.4	$20 < p_T < 80$	1.0	0.007	13.5
50–90% Pb–Pb	0.2	$14 < p_T < 40$	0.51	0.50	13.2
50–90% Pb–Pb	0.4	$10 < p_T < 40$	0.54	0.31	12.4
50–70% Pb–Pb	0.2	$14 < p_T < 40$	0.53	0.50	13.4
50–70% Pb–Pb	0.4	$10 < p_T < 40$	0.58	0.29	12.4
70–90% Pb–Pb	0.2	$14 < p_T < 40$	0.53	0.22	11.4
70–90% Pb–Pb	0.4	$14 < p_T < 40$	0.58	0.18	11.5
pp	0.2	$11 < p_T < 40$	0.40	0.29	14.2
pp	0.4	$11 < p_T < 40$	0.44	0.33	13.6

5 Systematic uncertainties

This section collects summary figures for the different sources of systematic uncertainty estimated for the purity, cross section, and yield ratios in Sect. 5.1. Also, the total uncertainty calculation of yield ratios in pp collisions with different \sqrt{s} is discussed in Sect. 5.2, and the uncertainties for the yield ratios with different R are shown in 5.3, and for the R_{AA} in Sect. 5.4.

5.1 Purity, cross section, and normalisation

The systematic uncertainties on the normalisation of the cross section, which are the combination of three sources (minimum bias trigger cross section, $\langle N_{\text{coll}} \rangle$, and trigger rejection factor, see Ref. [1] for details) are reported in Table 4.

Table 4: Normalisation relative uncertainty sources in per cent of the cross section p_{T}^{γ} spectra. When two values are given, they relate to p_{T}^{γ} below or above 12 GeV/ c . The last row gives the combination of uncertainties used in the data-over-theory ratio of Figs. 14(b) and 15(b) of Ref. [1] and of Fig. 25 in this note.

Norm. unc. (%)	Pb–Pb	Pb–Pb	Pb–Pb	Pb–Pb	Pb–Pb	Pb–Pb	pp
Source	0–10%	10–30%	30–50%	50–90%	50–70%	70–90%	
$\sigma_{\text{MB}}^{\text{col. system}}$	0.9	0.9	0.9	0.9	0.9	0.9	2.1
$\langle N_{\text{coll}} \rangle$	1.1	0.9	1.2	1.6	1.8	1.8	–
$RF_{\epsilon_{\text{trig}}}$	–, 0.2	–, 0.4	–, 0.6	0.8, 1.0	1.1, 1.4	3.4, 4.5	1.6, 1.6
$\sigma_{\text{MB}}^{\text{col. system}} \times RF_{\epsilon_{\text{trig}}} / \langle N_{\text{coll}} \rangle$	1.4, 1.4	1.3, 1.3	1.5, 1.6	2.0, 2.0	2.3, 2.5	3.5, 4.5	2.6, 2.6

The uncertainties on the purity are shown in Figs. 14 ($R = 0.2$) and 15 ($R = 0.4$). The contributions of the individual sources of systematic uncertainty are displayed in the table and the figures, along with the statistical uncertainty and the total one. The uncertainties (systematic source-by-source, total systematic, and statistical) on the p_{T}^{γ} -differential cross section are shown in Figures 16 ($R = 0.2$) and 17 ($R = 0.4$). Figs. 18 and 19 show the uncertainties for the 50–90% Pb–Pb centrality class. Figures 16, 17 and 19 include points labelled as “other systematic” that correspond to the quadratic sum of the uncertainty sources with small or no dependence on p_{T}^{γ} and values at most at 2.5%: material budget, time, trigger efficiency, energy scale, CPV, and distance to masked channels. A detailed discussion on the different sources of systematic uncertainty and the methods used for their estimation can be found in Ref. [1].

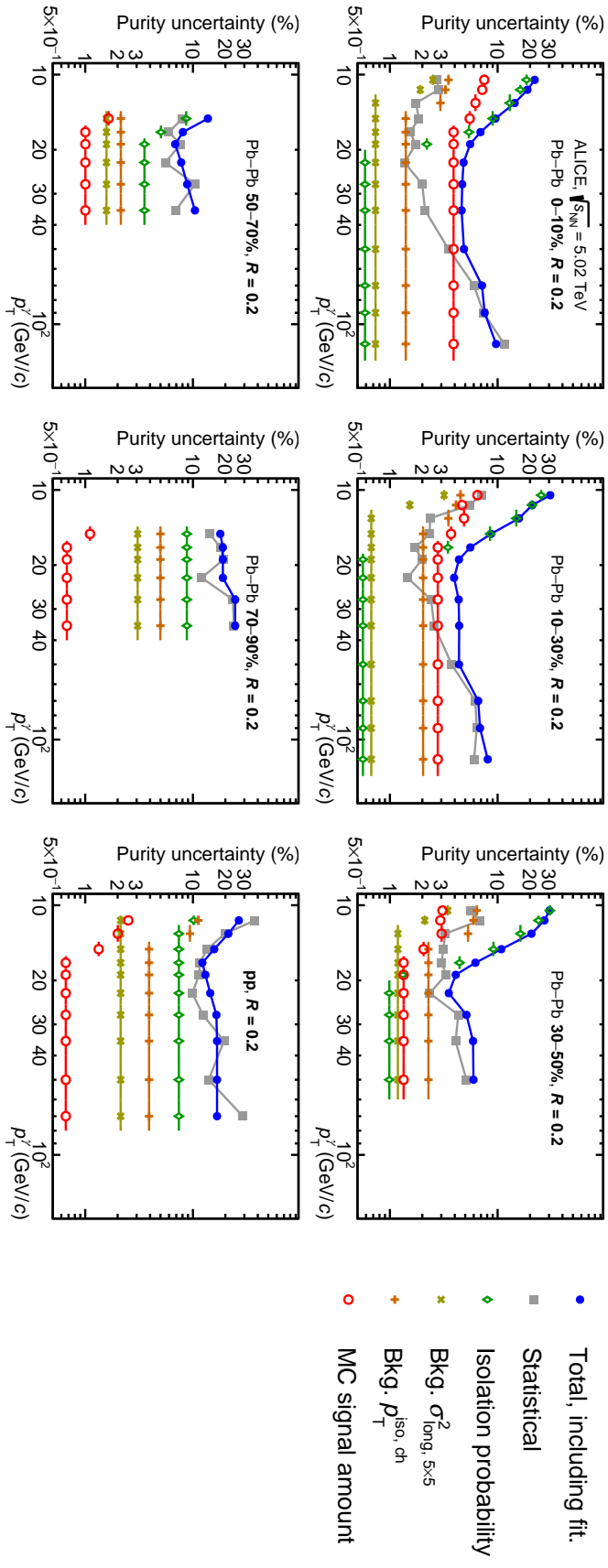


Fig. 14: (colour online) Contributions to the systematic uncertainty of the isolated-photon purity and their quadratic sum as a function of p_T^γ for $R = 0.2$, in pp (lower right frame) and in five Pb-Pb collisions centrality classes. The statistical uncertainty (grey squares) is also shown and may appear larger than the total uncertainty (blue dots) because of the smoothening done by the fit variation discussed in the text.

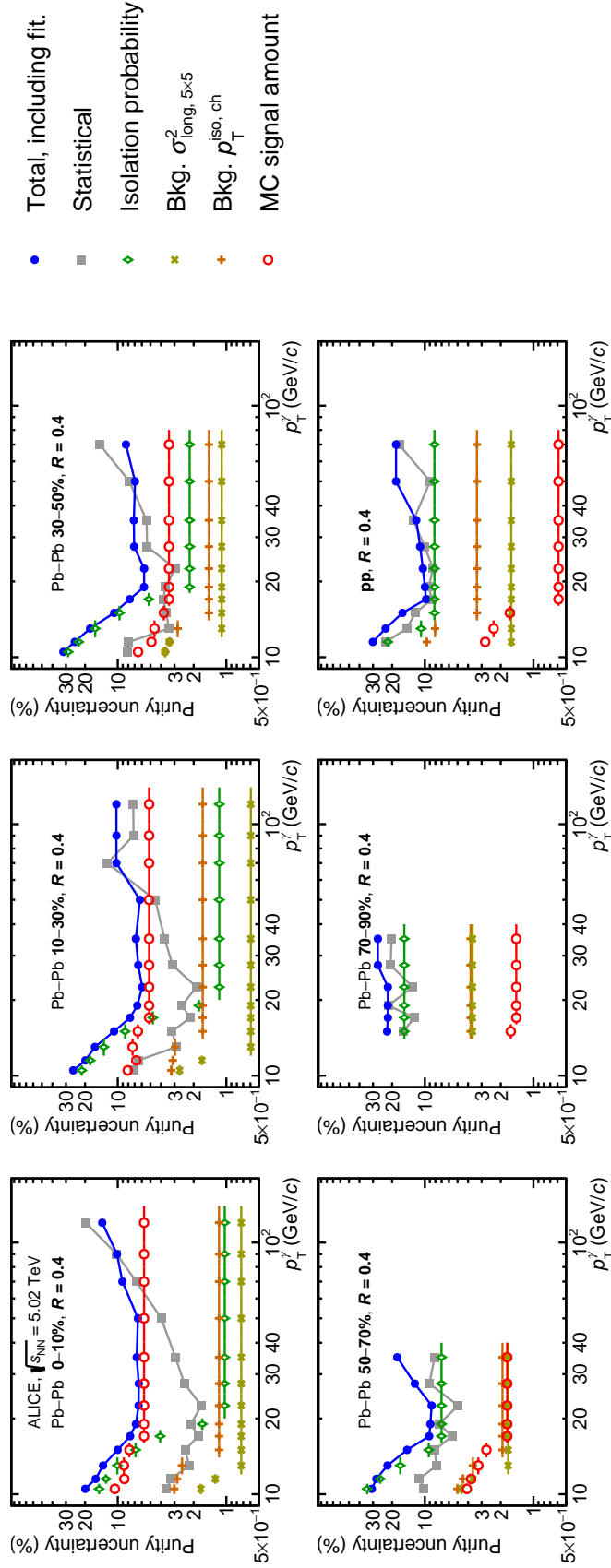


Fig. 15: (colour online) Contributions to the systematic uncertainty of the isolated-photon purity and their quadratic sum as a function of p_T^γ for $R = 0.4$, in pp (lower right frame) and in five Pb–Pb collisions centrality classes. The statistical uncertainty (grey squares) is also shown and may appear larger than the total uncertainty (blue dots) because of the smoothing done by the fit variation discussed in the text.

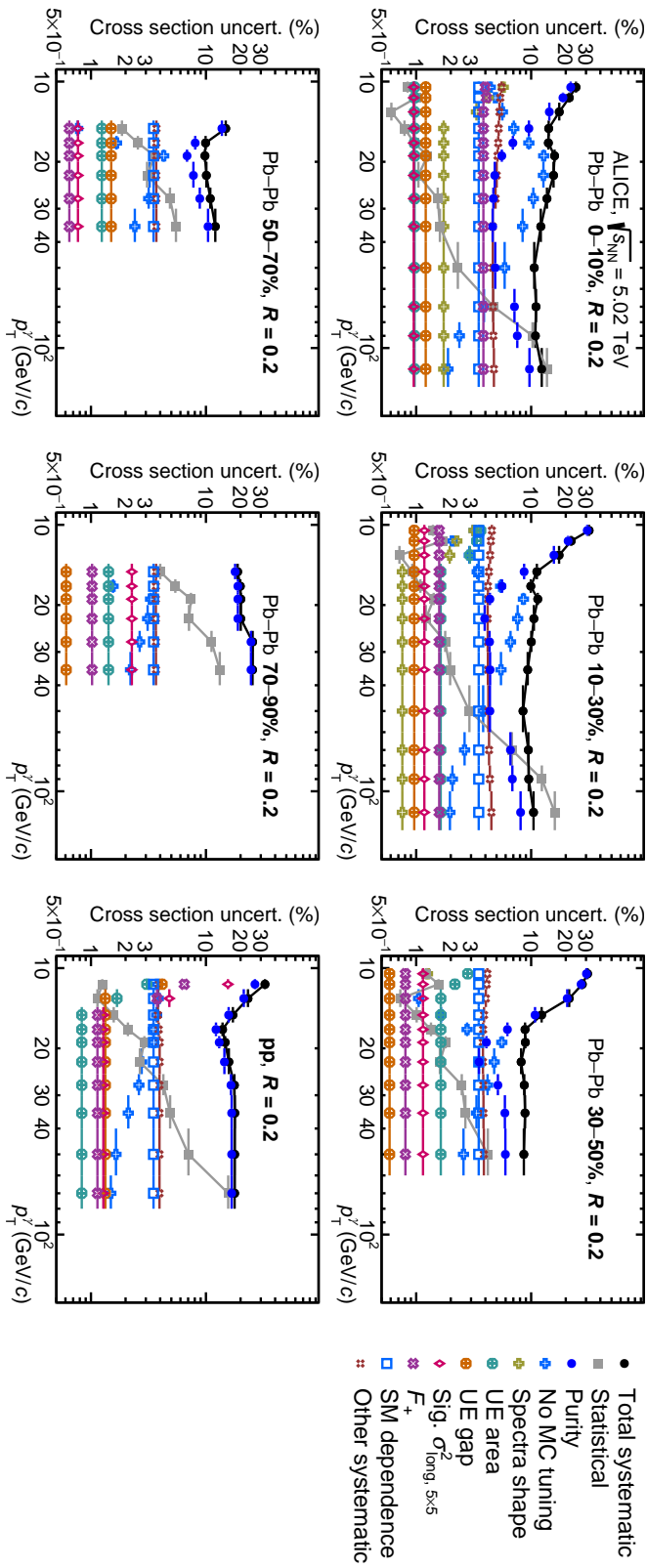


Fig. 16: (colour online) Contributions to the systematic uncertainty of the isolated-photon cross section and their quadratic sum as a function of p_T^γ for $R = 0.2$ in pp (lower right frame) and Pb-Pb collisions, the latter in five centrality classes. Total uncertainty (black dots) is calculated as the quadratic sum of all of the inputs. The statistical uncertainty (grey squares) is also shown.

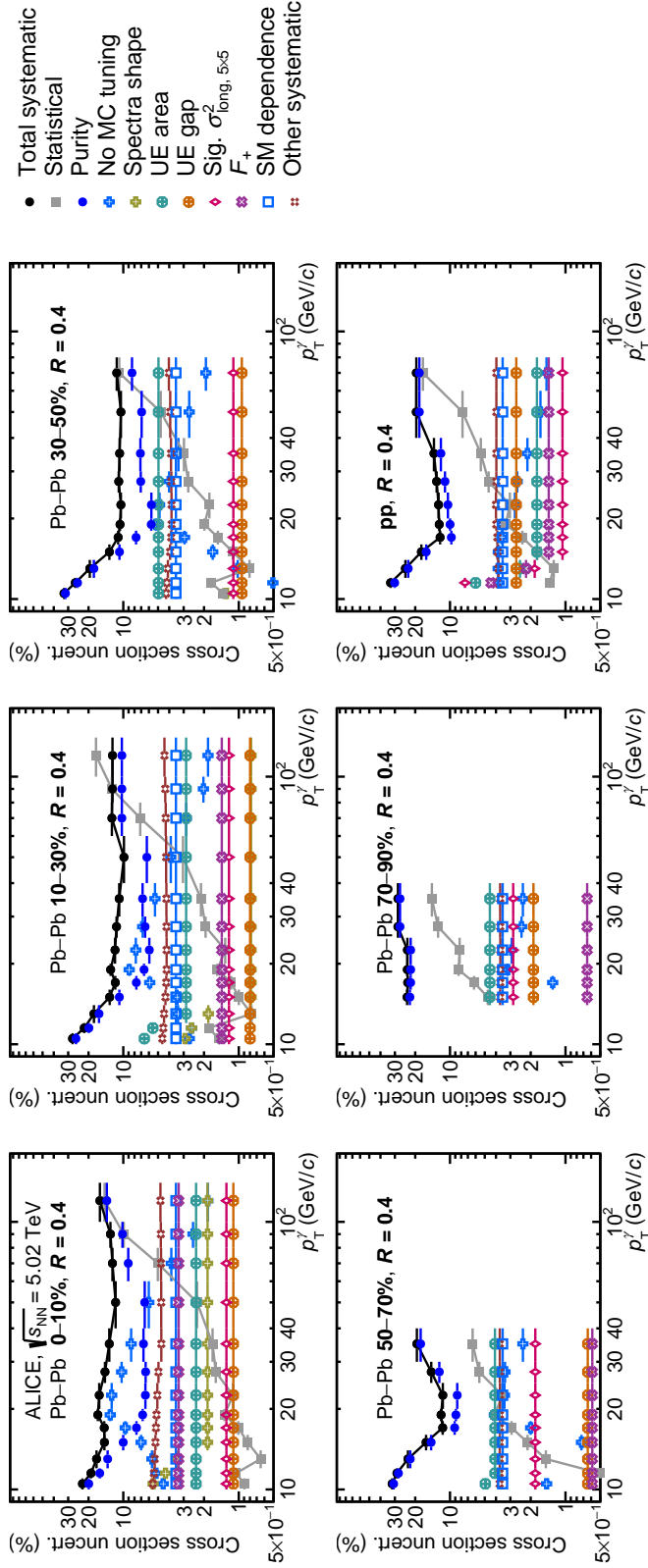


Fig. 17: (colour online) Contributions to the systematic uncertainty of the isolated-photon cross section and their quadratic sum as a function of p_T^γ for $R = 0.4$ in pp (lower right frame) and Pb–Pb collisions, the latter in five centrality classes. Total uncertainty (black dots) is calculated as the quadratic sum of all of the inputs. The statistical uncertainty (grey squares) is also shown.

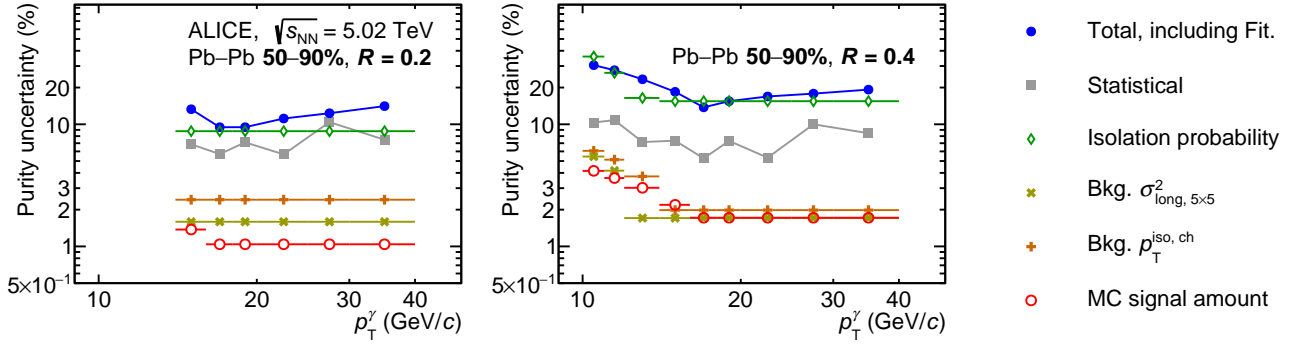


Fig. 18: (colour online) Contributions to the systematic uncertainty of the isolated-photon purity and their quadratic sum as a function of p_T^γ for $R = 0.2$ and $R = 0.4$, in Pb–Pb collisions for the 50–90% centrality class. The statistical uncertainty (grey squares) is also shown.

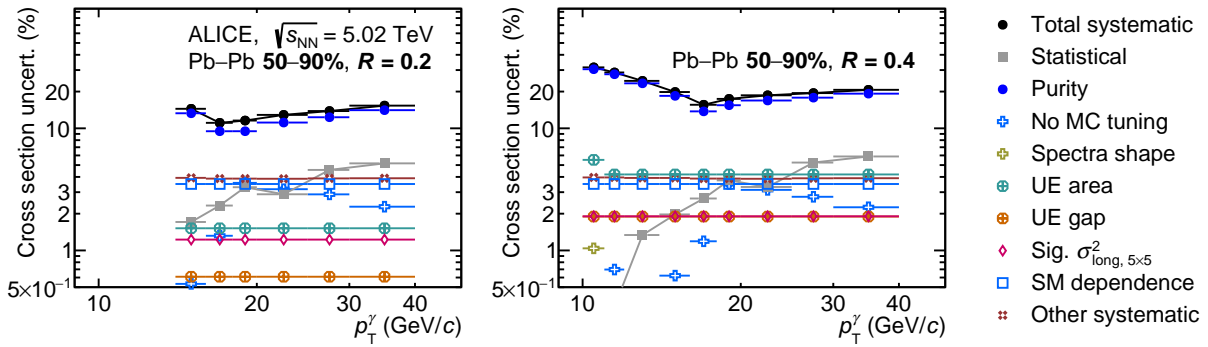


Fig. 19: (colour online) Contributions to the systematic uncertainty of the isolated-photon cross section and their quadratic sum as a function of p_T^γ for $R = 0.2$ and $R = 0.4$, in Pb–Pb collisions for the 50–90% centrality class. Total uncertainty (black dots) is calculated as the quadratic sum of all of the inputs. The statistical uncertainty (grey squares) is also shown.

5.2 pp collisions cross sections ratio at different centre-of-momentum energies

Figure 17 of Ref. [1] shows the ratio of the measured isolated-photon production cross sections in pp collisions at $\sqrt{s} = 13$ TeV (from [4]) over $\sqrt{s} = 5.02$ TeV, $f_{\sqrt{s}}\left(\frac{13}{5.02}\right)$, and of $\sqrt{s} = 7$ TeV (from [3]) over $\sqrt{s} = 5.02$ TeV, $f_{\sqrt{s}}\left(\frac{7}{5.02}\right)$, in data along with the corresponding ratios from JETPHOX NLO pQCD calculations described in Ref. [1]. All these measurements and calculations were done for a cone radius $R = 0.4$.

Not all the systematic uncertainties cancel in this ratio: since both the $\sqrt{s} = 7$ and 13 TeV measurements were done without UE subtraction, the full ‘‘gap and area UE’’ uncertainties from the $\sqrt{s} = 5.02$ TeV measurement are used. Also, the clusters were selected depending on their number of local maxima, which is not applicable in this analysis due to the growth restriction when aggregating cells to the cluster that can only generate clusters with one local maximum, so the corresponding uncertainty is taken from those measurements fully. Since there is no CPV selection for the $\sqrt{s} = 5.02$ TeV measurement, both CPV uncertainties from the previous measurements are taken as well. Since the ‘‘isolation probability’’ source uncertainty is expected to cancel partially, we chose to take half of the denominator uncertainty for the ratio. Finally, the ‘‘SM dependent’’ uncertainty does not cancel in the ratio $f_{\sqrt{s}}\left(\frac{7}{5.02}\right)$, since the SM behaviour can change per running period and the acceptances were very different: no DCal and $|\eta| < 0.27$ for the $\sqrt{s} = 7$ TeV sample. It was taken as the quadratic sum of the SM-dependent uncertainty: $3.5\% \times \sqrt{2} = 4.9\%$. For the ratio $f_{\sqrt{s}}\left(\frac{13}{5.02}\right)$, the data-taking periods were close and it was considered that the SM performance does not change. All these remaining systematic sources are added in quadrature, resulting in an uncertainty on the ratio $f_{\sqrt{s}}\left(\frac{13}{5.02}\right)$ that ranges between 6.4% and 9.2% depending on p_{T}^{γ} , and in an uncertainty on the ratio $f_{\sqrt{s}}\left(\frac{7}{5.02}\right)$ between 7.7% and 14%. Due to the small size of the $\sqrt{s} = 7$ TeV dataset, the dominant uncertainty in the ratio $f_{\sqrt{s}}\left(\frac{7}{5.02}\right)$ is the statistical one, which ranges from 15% to 40% depending on p_{T}^{γ} . For the ratio $f_{\sqrt{s}}\left(\frac{13}{5.02}\right)$, the statistical uncertainty is smaller than the systematic uncertainty and ranges from 2–4% at low p_{T}^{γ} up to 8% in the highest p_{T}^{γ} interval.

The normalisation scale uncertainty is not added to the systematic uncertainty. It is calculated from the luminosity of the two measurements, and is found to be equal to 3.2% for the ratio $f_{\sqrt{s}}\left(\frac{13}{5.02}\right)$, with a similar contribution from each dataset, and to 10% for the ratio $f_{\sqrt{s}}\left(\frac{7}{5.02}\right)$, again dominated by the $\sqrt{s} = 7$ TeV uncertainty.

The NLO pQCD scale uncertainty decreases with p_{T}^{γ} from 7% to 3% in the ratio $f_{\sqrt{s}}\left(\frac{13}{5.02}\right)$, and from 2% to 1% in the ratio $f_{\sqrt{s}}\left(\frac{7}{5.02}\right)$. The PDF uncertainty is smaller than the NLO pQCD scale one, decreasing from 2.7% to 1% for the ratio $f_{\sqrt{s}}\left(\frac{13}{5.02}\right)$ and from 1.6% to 0.7% for the ratio $f_{\sqrt{s}}\left(\frac{7}{5.02}\right)$.

5.3 Ratio of yields with different cone radius

Figure 20 compiles all the uncertainties for the ratio of the p_{T}^{γ} -differential cross sections with different cone radii, $f_{R\left(\frac{0.4}{0.2}\right)}$. Points in the figures labelled as ‘‘other systematic’’ correspond to the quadratic sum of the uncertainty sources with small or no dependence on p_{T}^{γ} and values at most at 2.5%: trigger efficiency, CPV, signal range for $\sigma_{\text{long}, 5 \times 5}^2$, the variation of F_+ , the spectral shape, the cross talk tuning, and the UE area and gap.

5.4 Nuclear modification factor

Figures 21 ($R = 0.2$) and 22 ($R = 0.4$) compile all the relative systematic uncertainties for the R_{AA} . Points in the figures labelled as ‘‘other systematic’’ correspond to the quadratic sum of the uncertainty sources with small or no dependence on p_{T}^{γ} and values at most at 2.5%: trigger efficiency, CPV, and the background ranges for the $p_{\text{T}}^{\text{iso, ch}}$ and $\sigma_{\text{long}, 5 \times 5}^2$.

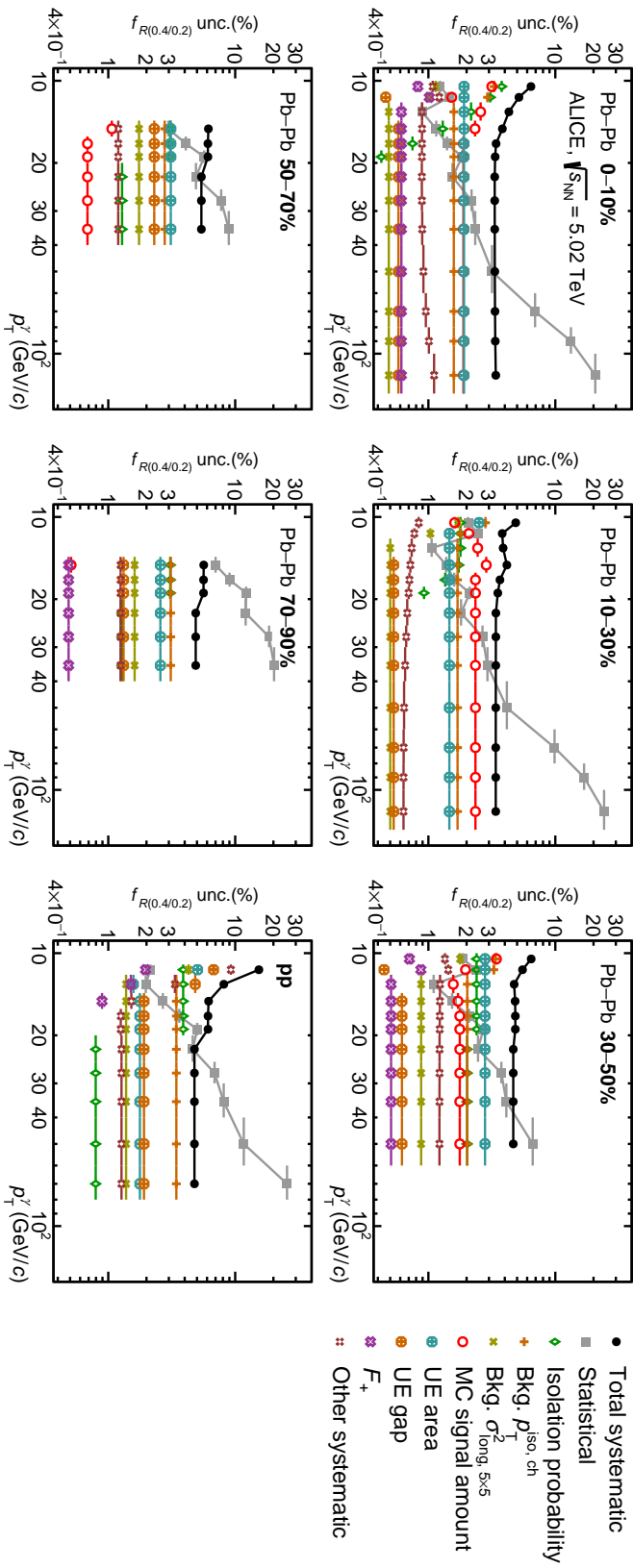


Fig. 20: for the ratio of cross sections with $R = 0.4$ and $R = 0.2$, $f_{R(0.4/0.2)}$, in per cent as a function of p_T^γ . Total uncertainty (black dots) is calculated as the quadratic sum of all of the sources. The statistical uncertainty (grey squares) is also shown.

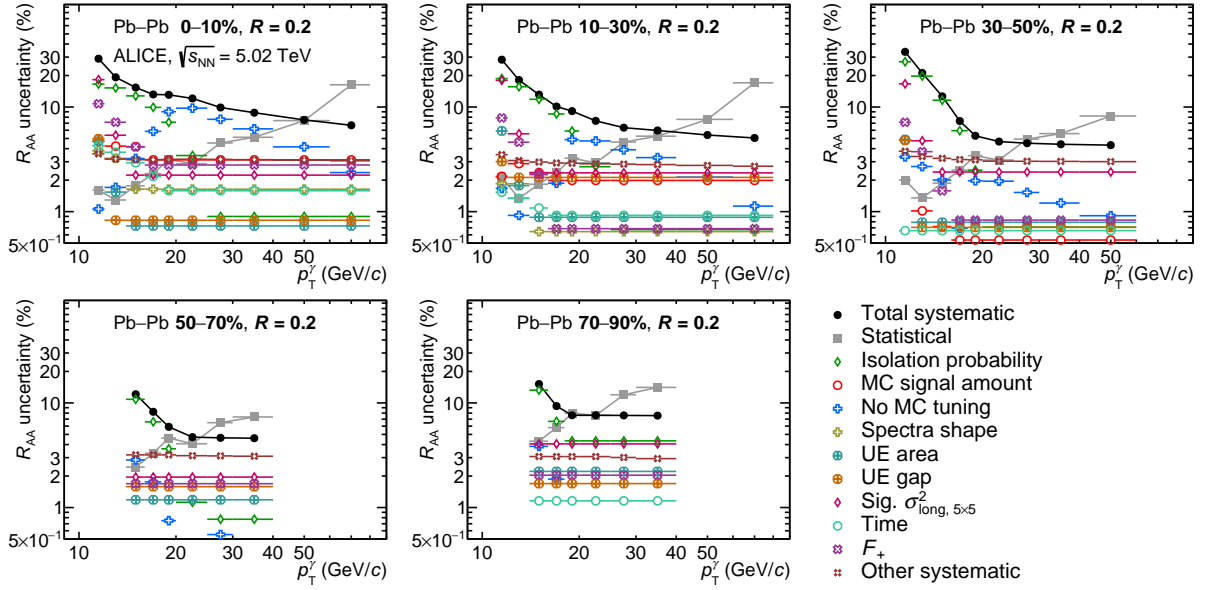


Fig. 21: Compilation of the systematic uncertainties for the calculation of the R_{AA} with $R = 0.2$. Total uncertainty (black dots) is calculated as the quadratic sum of all of the inputs. The statistical uncertainty (grey squares) is also shown.

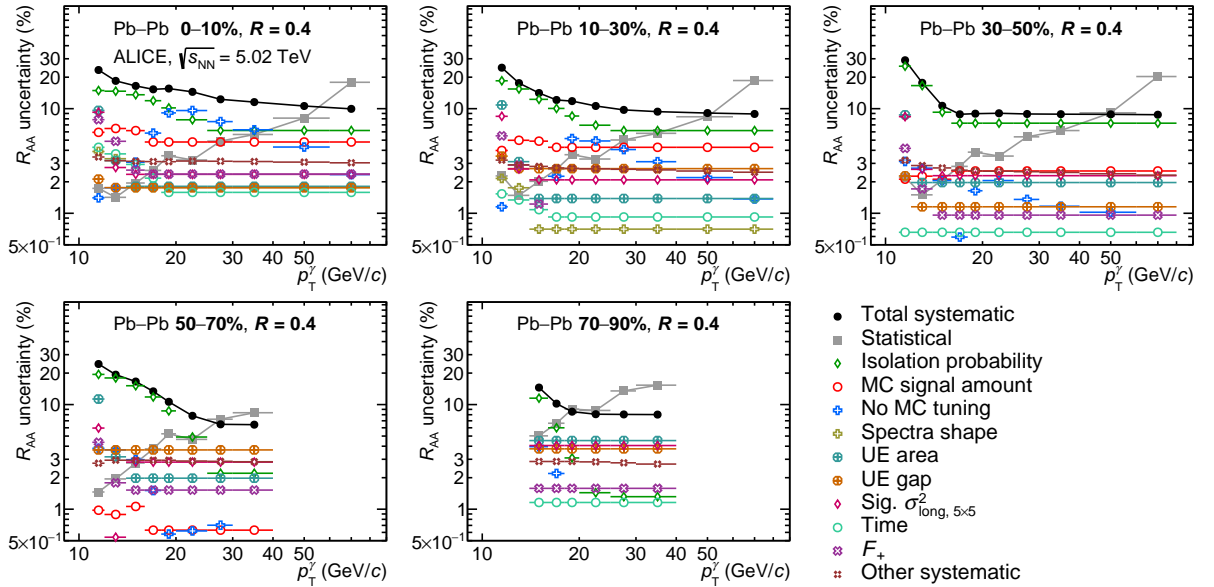


Fig. 22: Compilation of the systematic uncertainties for the calculation of the R_{AA} with $R = 0.4$. Total uncertainty (black dots) is calculated as the quadratic sum of all of the inputs. The statistical uncertainty (grey squares) is also shown.

6 Results

6.1 Nuclear modification factor using pQCD NLO as pp collisions

Figure 23 shows the R_{AA} calculated from the measured cross sections in Pb–Pb collisions using as denominator the cross section calculated with JETPHOX at NLO for pp collisions instead of the measured one. This $R_{AA}^{\text{pp col.: NLO pQCD}}$ and the ratio of the calculated cross sections with JETPHOX using nPDF (Pb–Pb collisions) over PDF (pp collisions) without centrality selection are closer than in Fig. 16 of Ref. [1] as expected from the reported data over theory ratios in Figs. 12 and 13 of Ref. [1].

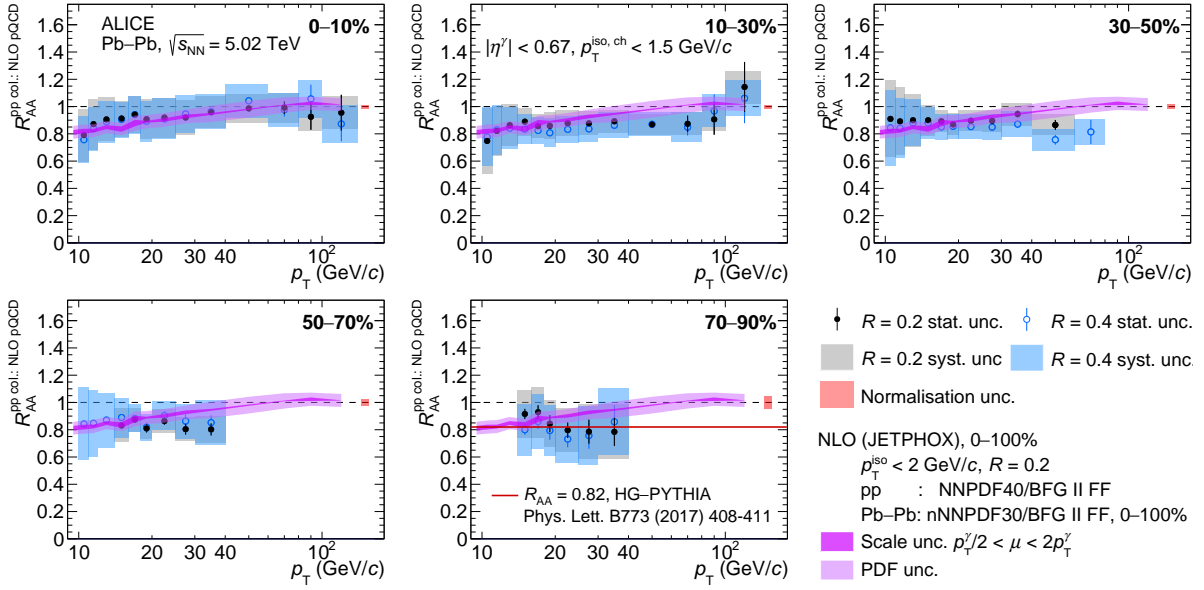


Fig. 23: (colour online) Nuclear modification factor R_{AA} for isolated photons at $\sqrt{s_{NN}} = 5.02$ TeV for isolation-cone radii $R = 0.2$ (black) and $R = 0.4$ (blue). In data, the denominator is replaced by the pp collisions NLO pQCD calculation with JETPHOX. Error bars and boxes are the statistical and systematic uncertainties, respectively. The bands correspond to pQCD calculations with JETPHOX for Pb–Pb collisions (nPDF) for 0–100% centrality over pp collisions (PDF). The width of each band corresponds to the scale and PDF uncertainties. The normalisation uncertainties are represented as a red box centred at unity. The solid line in the most peripheral centrality class 70–90% at $R_{AA} = 0.82$ corresponds to the HG-PYTHIA model expectation [12].

6.2 Pb–Pb collisions 50–90% centrality class

In Ref. [1], the centrality classes 50–70% and 70–90% are shown in most of the figures, but the result for their combination 50–90% is also discussed for the R_{AA} when comparing to the CMS experiment results. Here, we show the main results for the centrality class 50–90% for completeness.

Figure 24 shows the purity and efficiency for both values of the cone radii. The purity values found are very similar for both R and compatible with those of the 50–70% and 70–90% centrality class. The efficiency values are in between those of the 50–70% and 70–90% centrality classes as it can be seen by comparing Fig. 24-right with the corresponding panels in Fig. 8 of Ref. [1].

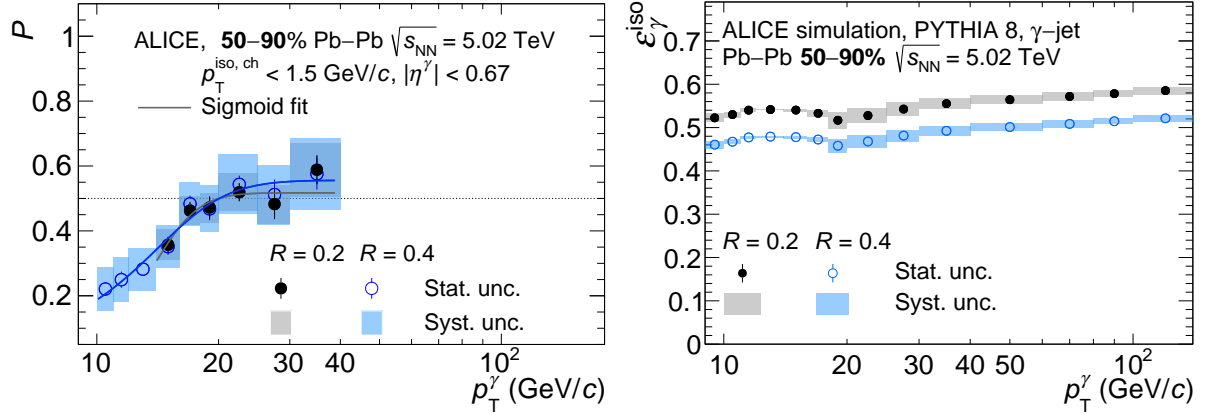


Fig. 24: (colour online) Isolated-photon purity (left) and efficiency (right) as a function of p_T^γ for peripheral Pb–Pb collisions in the 50–90% centrality class for $R = 0.2$ and $R = 0.4$. The points are shown with systematic and statistical uncertainties discussed in Sect. 4 of Ref. [1] and shown in figures in Sect. 5.1 of this note. The purity is calculated using Eq. (5) and is calculated adding in quadrature all the sources shown in Fig. 18. The lines in the purity plot are the result of the fit with two sigmoid functions, Eq. (8), for each cone radius. The efficiency is obtained as explained in Sect. 3.5 of Ref. [1].

Analogous to Figs. 14 and 15 in Ref. [1], Fig. 25 shows the p_T^γ -differential cross section for the 50–90% centrality class. The cross sections for the two cone radii are shown in Fig. 25-left. Table 5 lists the luminosity and trigger normalisation parameters used to obtain the cross sections with the corresponding uncertainties. The ratio data-to-theory is displayed in Fig. 25-right. A fair agreement with theory is seen although most points tend to be below unity like for the 70–90% centrality class in Ref. [1]. The theory calculation is an NLO pQCD calculation from JETPHOX 1.3.1 [13, 14]. The fragmentation function used is BFG II [15], and the nuclear parton distribution function is nNNPDF3.0 [16], which has been calculated for 0–100% centrality. The theory calculation is scaled by $\langle N_{\text{coll}} \rangle = 38.4 \pm 0.6$ for the centrality class 50–90%, obtained from Ref. [17].

Table 5: Trigger $RF_{\epsilon_{\text{trig}}^{\text{trig}}}$ (Eq. (8) of Ref. [1]), $\mathcal{L}_{\text{NN}}^{\text{trig}}$, and $\mathcal{L}_{\text{int}}^{\text{trig}}$ (Eq. (9) of Ref. [1]) for 50–90% Pb–Pb collisions per trigger inclusive cluster p_T range. The $\mathcal{L}_{\text{NN}}^{\text{trig}}$ uncertainty contains both the AA inelastic cross section $\sigma_{\text{NN}}^{\text{INEL}}$ and rejection factor uncertainties. The integrated luminosity uncertainty includes in addition the $\langle N_{\text{coll}} \rangle$ uncertainty. See definitions of the different parameters in Ref. [1].

Trigger	p_T (GeV/c)	$RF_{\epsilon_{\text{trig}}^{\text{trig}}}$	$\mathcal{L}_{\text{NN}}^{\text{trig}}$ (nb $^{-1}$)	$\mathcal{L}_{\text{int}}^{\text{trig}}$ (nb $^{-1}$)
MB+L1- γ -low	$p_T < 12$	117.2 ± 1.2	7.02 ± 0.08	270 ± 5
MB+L1- γ -high+low	$p_T > 12$	158.4 ± 1.8	9.83 ± 0.12	378 ± 8

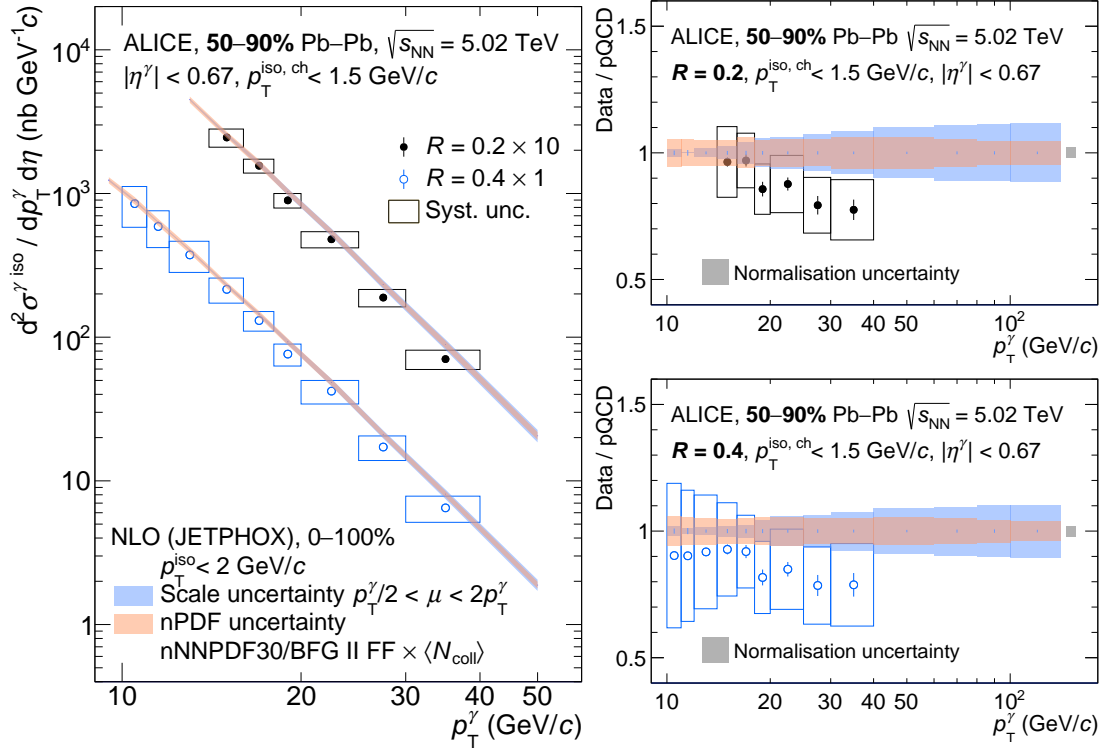


Fig. 25: (colour online) Left: Isolated-photon differential cross section measured in Pb–Pb collisions at $\sqrt{s_{NN}} = 5.02$ TeV for the 50–90% centrality class, for $R = 0.2$ (scaled by a factor 10) and $R = 0.4$ (not scaled). Error bars and boxes are the statistical and systematic uncertainties, respectively. The bands correspond to NLO pQCD calculations with JETPHOX, for Pb–Pb collisions calculated for the 0–100% centrality class but scaled by $\langle N_{\text{coll}} \rangle$. Right: Ratio of data over JETPHOX NLO pQCD calculations for $R = 0.2$ (top) and $R = 0.4$ (bottom). The bands centred at unity correspond to the JETPHOX NLO pQCD calculation uncertainties. The normalisation uncertainty of 2% is not included in the left panel but it is shown as a grey box in the right of each frame around unity.

Figure 26 shows the ratio of the cross sections with different R , like Fig. 14 in Ref. [1]. This ratio is at about 0.9 and is in agreement with the pQCD NLO calculation.

Figure 27 shows the modified R_{AA} where the denominator is replaced by the JETPHOX NLO pQCD calculation for pp collisions like in Fig. 23. This ratio is at about 0.8 for most points, but still in agreement with the HG-PYTHIA model that expects a value of 0.91. The results for both R values are in good agreement.

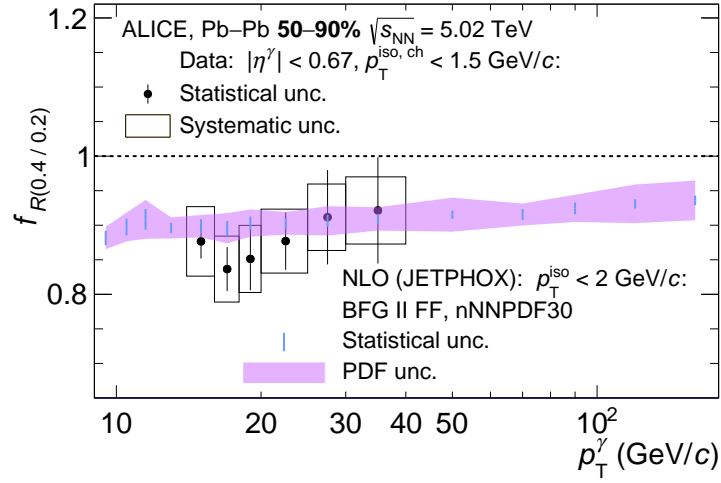


Fig. 26: (colour online) Ratio of isolated-photon p_{T}^γ -differential cross sections measured with $R = 0.4$ over $R = 0.2$, $f_{R(0.4/0.2)}$, for Pb–Pb collisions at $\sqrt{s_{\text{NN}}} = 5.02$ TeV and for the 50–90% centrality class. Error bars and boxes are the statistical and systematic uncertainties, respectively. The pink band corresponds to pQCD calculations with JETPHOX, the width represents the PDF uncertainty, and the blue vertical bars indicate the statistical uncertainty of the calculations.

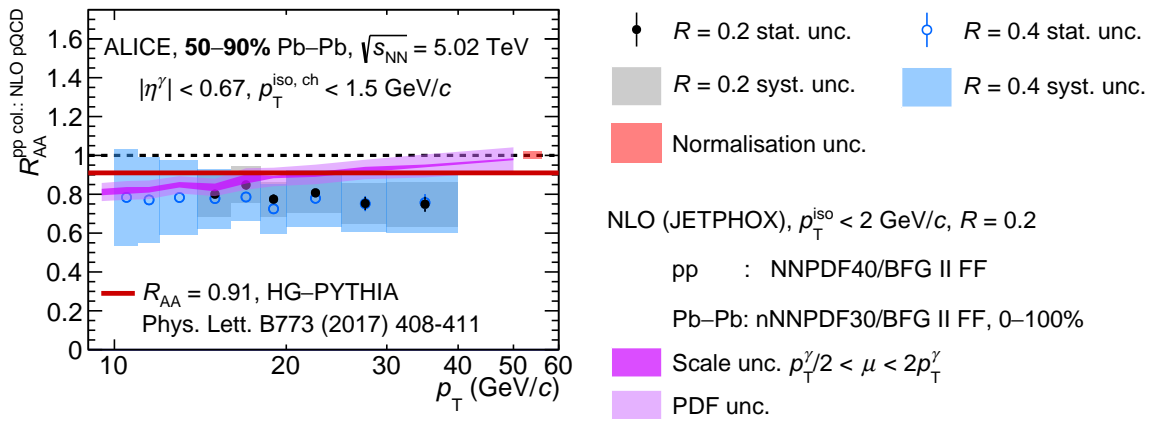


Fig. 27: (colour online) Nuclear modification factor R_{AA} for isolated photons at $\sqrt{s_{\text{NN}}} = 5.02$ TeV for the 50–90% centrality class, and for isolation-cone radii $R = 0.2$ (black) and $R = 0.4$ (blue). In data, the denominator is replaced by the pp collisions NLO pQCD calculation with JETPHOX. Error bars and boxes are the statistical and systematic uncertainties, respectively. The bands correspond to pQCD calculations with JETPHOX for Pb–Pb collisions (nPDF) for 0–100% centrality over pp collisions (PDF). The width of each band corresponds to the scale and PDF uncertainties. The normalisation uncertainties are represented as a red box centred at unity. The solid line in the most peripheral centrality class 70–90% at $R_{\text{AA}} = 0.91$ corresponds to the HG-PYTHIA model expectation [12].

6.3 Nuclear modification factor in ALICE and CMS

Figure 28 compares the R_{AA} measured by ALICE and CMS for $R = 0.4$, equivalent to Fig. 17 of Ref. [1] where the result for $R = 0.2$ from ALICE is also shown. In addition, the theory R_{AA} is also shown here. The good agreement between CMS and ALICE points is displayed.

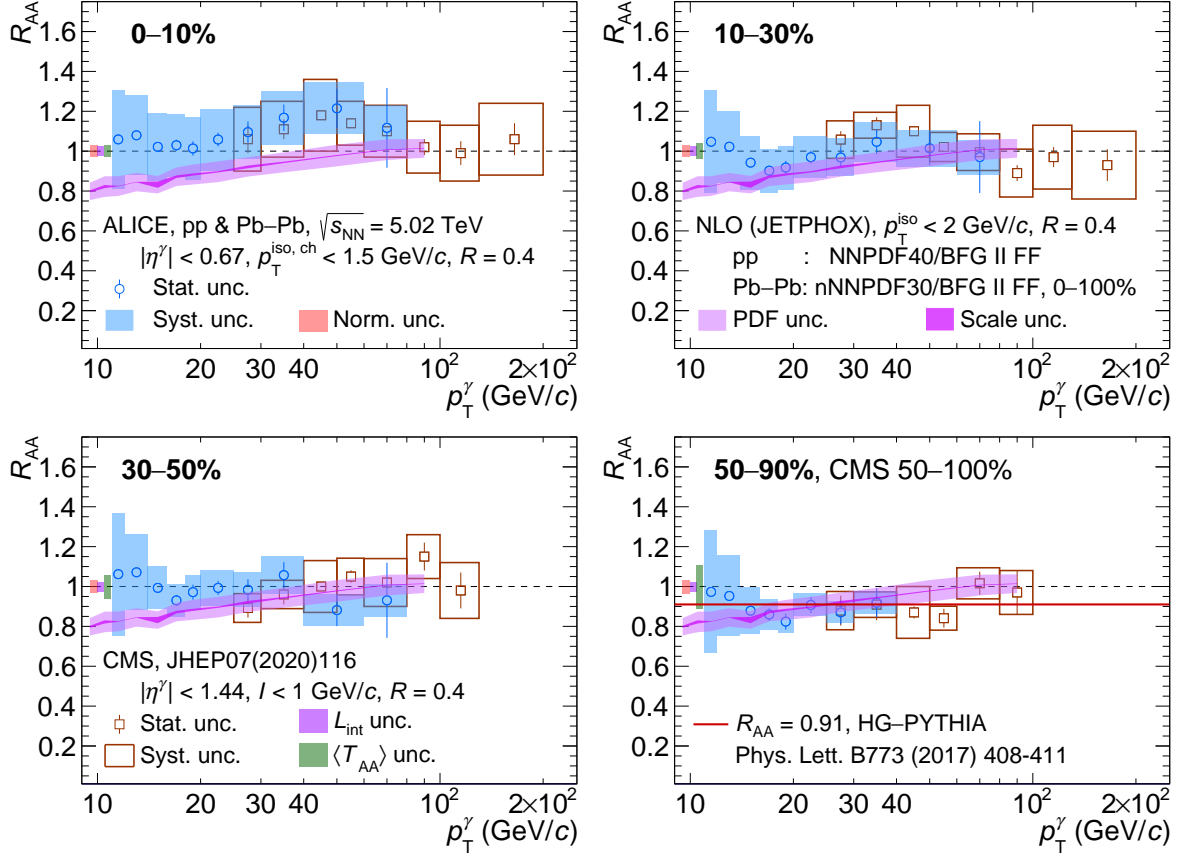


Fig. 28: (colour online) Nuclear modification factor R_{AA} for isolated photons measured by ALICE and CMS [18] for isolation-cone radius $R = 0.4$ at $\sqrt{s_{NN}} = 5.02$ TeV and for four centrality classes. Error bars and boxes are the statistical and systematic uncertainties, respectively. The solid line in the peripheral centrality class 50–90% at $R_{AA} = 0.91$, is the result of the HG-PYTHIA model [12]. The ALICE normalisation uncertainties are represented as a red box centred at unity. For CMS, the normalisation uncertainties are displayed as a violet box for the integrated luminosity and a green box for the nuclear overlap function $\langle T_{AA} \rangle = \langle N_{\text{coll}} \rangle / \sigma_{NN}^{\text{INEL}}$. The bands correspond to pQCD calculations with JETPHOX for Pb–Pb collisions (nPDF) for 0–100% centrality over pp collisions (PDF). The width of each band corresponds to the scale and PDF uncertainties.

6.4 Comparison of the isolated photon and Z boson cross section and nuclear modification factor as a function of the centrality class: Check of the binary scaling factor

Electroweak particles are not expected to be modified by the quark–gluon plasma produced in Pb–Pb collisions, thus, their measurement is considered a benchmark to validate the nucleon–nucleon binary collision scaling, $\langle N_{\text{coll}} \rangle$, calculated via the Glauber model [19]. If the scaling calculated by the Glauber model was adequate, the R_{AA} (see definition in Ref. [1]) of Z^0 bosons and isolated photons must be at unity. In Ref. [12] where the HG-PYTHIA model is presented, it is discussed that the presence of jets and other geometrical effects in peripheral collisions biases the experimental measurements of the centrality classes via particle multiplicity of the event and needs a correction.

Figure 29-left shows the cross section for isolated photons and Z^0 bosons from CMS [20] as a function of centrality and scaled by $\langle N_{\text{coll}} \rangle$ (photons) or $\langle T_{AA} \rangle = \langle N_{\text{coll}} \rangle / \sigma_{\text{INEL}}^{\text{AA}}$ with $\sigma_{\text{INEL}}^{\text{AA}}$ the AA inelastic cross section (Z^0 bosons). Isolated photons are measured in the range $20 < p_T^\gamma < 25$ GeV/c, which is the p_T^γ interval with the smallest total systematic plus statistical uncertainty. The points are extracted from Fig 14 and 15 of Ref. [1]. The Z^0 bosons cross section is reported in Ref. [20] and is integrated over p_T .

Figure 29-right shows the R_{AA} for isolated photons (extracted from Fig. 20 of Ref. [1]), together with ratio of the cross sections in each centrality class to the one in 0–90% centrality class for the Z^0 boson (the systematic uncertainty is taken from the numerator). Both ratios are not strictly the same but should be equally sensitive to the validity of the $\langle N_{\text{coll}} \rangle$ scaling.

The figures show that the $\langle N_{\text{coll}} \rangle$ scaling works in the centrality range 0–70%, the scaled cross section is the same for the different centrality classes and the R_{AA} agrees with unity. In the 70–90% centrality class, both the ALICE isolated photon and the CMS Z^0 boson measurements show a deviation of the ratio with respect to the other Pb–Pb collisions centrality classes. Both deviations are found to agree with the HG-PYTHIA model, see [20] for the CMS Z^0 bosons measurement ratio to the model.

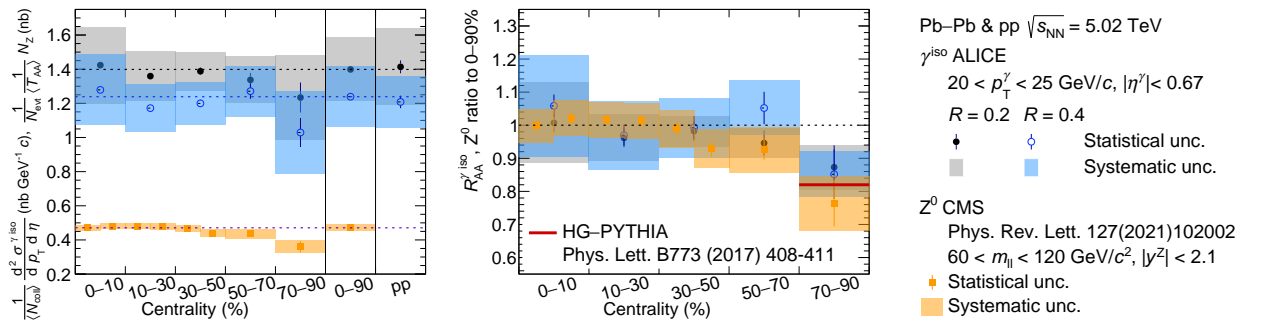


Fig. 29: (colour online) Left: Cross section of isolated photons with $20 < p_T^\gamma < 25$ GeV/c for $R = 0.2$ and 0.4 as a function of the centrality class or collision system, in Pb–Pb and pp collisions at $\sqrt{s_{NN}} = 5.02$ TeV from Figs. 14 and 15 of Ref. [1]. Also shown is the p_T^γ -integrated cross section of Z^0 bosons measured by CMS [20] for Pb–Pb collisions at $\sqrt{s_{NN}} = 5.02$ TeV. The 0–90% centrality class for isolated photons is calculated as the $\langle N_{\text{coll}} \rangle$ weighted average of the other centrality classes. The dotted lines indicate the value of the 0–90% centrality class centre. Right: R_{AA} for isolated photons from Fig. 18 of Ref. [1] and ratio of the Z^0 boson cross sections in each centrality class to the one in 0–90%. The solid line in peripheral centrality class 70–90% at $R_{AA} = 0.82$ corresponds to the expectation from the HG-PYTHIA model [12].

6.5 Ratio of isolated-photon cross sections in Pb–Pb collisions: central to semi-central or semi-peripheral

The comparison of the isolated photon production in the different Pb–Pb centrality classes, through the ratios of the yields in (more) central over (more) peripheral collisions, offers experimental advantages: first, because the systematic uncertainty cancellation is stronger than in the R_{AA} , in particular for close centrality classes; and second, because the p_T^γ range can be pushed to slightly lower values than for the R_{AA} in some ratios.

Due to the centrality selection bias as well as to the poor statistics and smaller p_T^γ range, the 70–90% centrality class was not considered as a reference. The 50–70% class was used as a semi-peripheral reference instead, and 30–50% as a semi-central reference. The following ratios were defined, in which k denotes the centrality class index

$$R_{\text{CSP}} = \frac{\langle N_{\text{coll}} \rangle^{50-70\%}}{\langle N_{\text{coll}} \rangle^k} \frac{d^2 \sigma_{\text{Pb-Pb}}^{\gamma \text{ iso}} / (dp_T d\eta)|_k}{d^2 \sigma_{\text{Pb-Pb}}^{\gamma \text{ iso}} / (dp_T d\eta)|_{50-70\%}}, \quad R_{\text{CSC}} = \frac{\langle N_{\text{coll}} \rangle^{30-50\%}}{\langle N_{\text{coll}} \rangle^k} \frac{d^2 \sigma_{\text{Pb-Pb}}^{\gamma \text{ iso}} / (dp_T d\eta)|_k}{d^2 \sigma_{\text{Pb-Pb}}^{\gamma \text{ iso}} / (dp_T d\eta)|_{30-50\%}}. \quad (9)$$

Figures 30 and 31 compile all the relative systematic uncertainties for the R_{CSP} and R_{CSC} ratios. Points in the figures labelled as “other systematic” correspond to the quadratic sum of the uncertainty sources with small or no dependence on p_T^γ and values at most at 2.5%: trigger efficiency, CPV, background ranges for the $p_T^{\text{iso, ch}}$ and $\sigma_{\text{long}, 5 \times 5}^2$, signal range for the $\sigma_{\text{long}, 5 \times 5}^2$, and the UE area and gap.

The R_{CSP} and R_{CSC} ratios are shown in Fig. 32 with the systematic and statistical uncertainties, they are compatible with unity as expected, and p_T^γ independent.

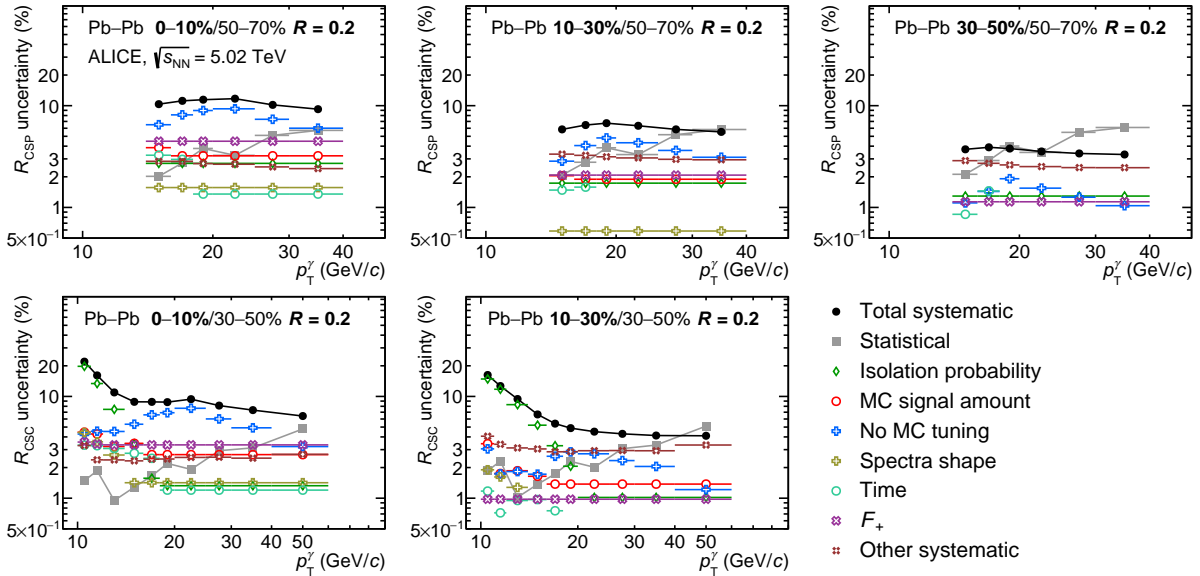


Fig. 30: Compilation of the systematic uncertainties for the calculation of the R_{CSP} (top) and R_{CSC} (bottom) with $R = 0.2$. Total uncertainty (black dots) is calculated as the quadratic sum of all of the inputs. The statistical uncertainty (grey squares) is also shown.

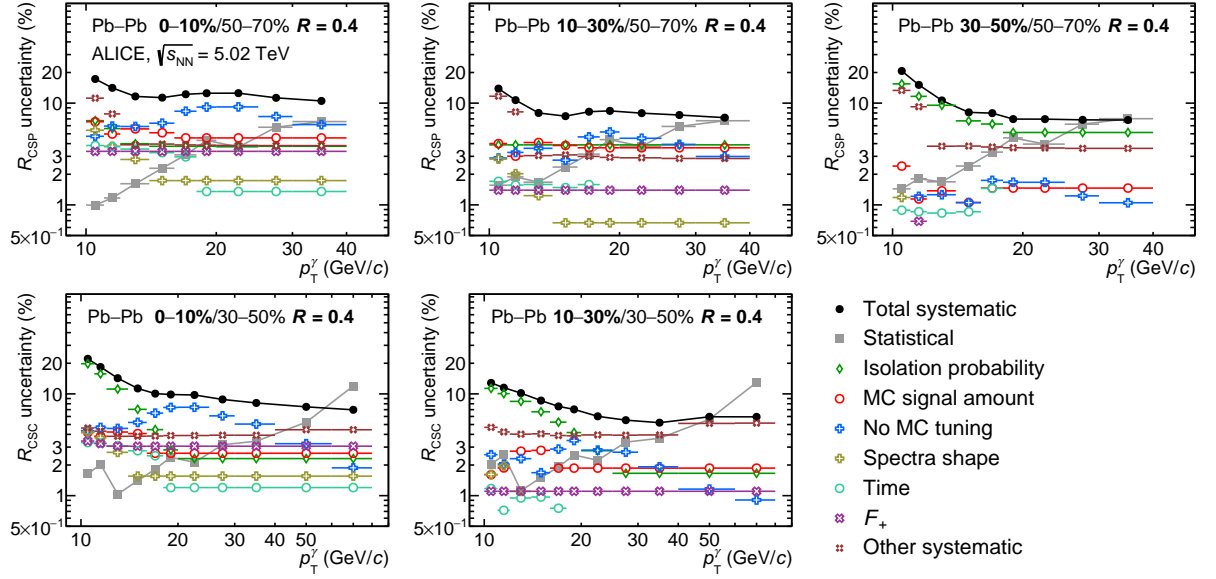


Fig. 31: Compilation of the systematic uncertainties for the calculation of the R_{CSP} (top) and R_{CSC} (bottom) with $R = 0.4$. Total uncertainty (black dots) is calculated as the quadratic sum of all of the inputs. The statistical uncertainty (grey squares) is also shown.

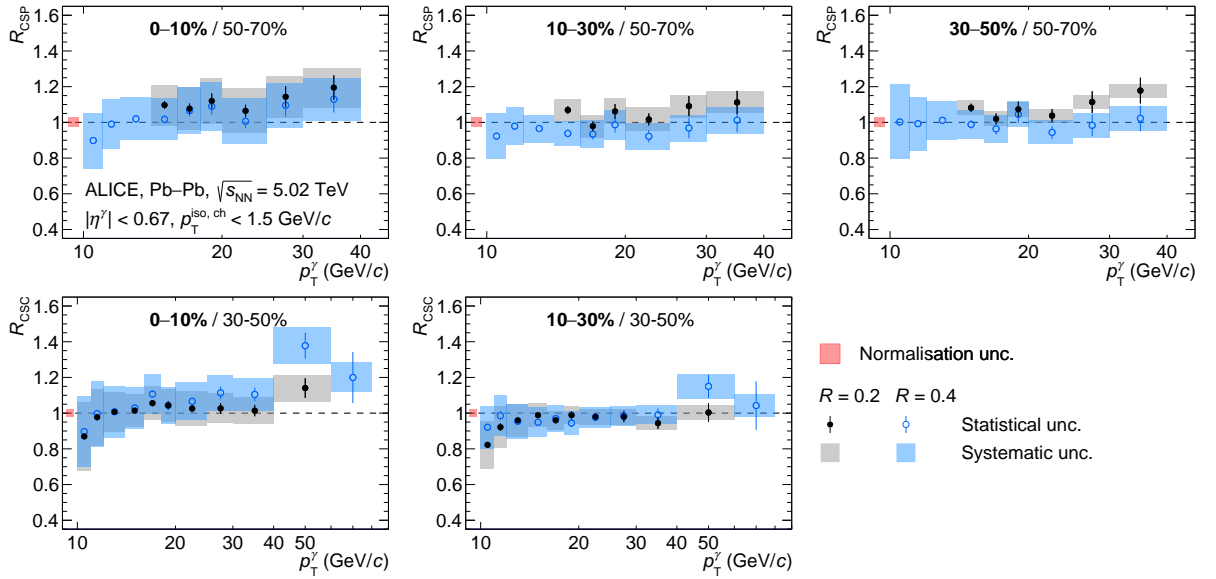


Fig. 32: (colour online) Ratio of the Pb–Pb isolated-photon yields, central (0–50%) over semi-peripheral (50–70%) on top, and central (0–30%) over semi-central (30–50%) on bottom, for isolation-cone radii $R = 0.2$ and 0.4 .

Acknowledgements

The ALICE Collaboration would like to thank all its engineers and technicians for their invaluable contributions to the construction of the experiment and the CERN accelerator teams for the outstanding performance of the LHC complex. The ALICE Collaboration gratefully acknowledges the resources and support provided by all Grid centres and the Worldwide LHC Computing Grid (WLCG) collaboration. The ALICE Collaboration acknowledges the following funding agencies for their support in building and running the ALICE detector: A. I. Alikhanyan National Science Laboratory (Yerevan Physics Institute) Foundation (ANSL), State Committee of Science and World Federation of Scientists (WFS), Armenia; Austrian Academy of Sciences, Austrian Science Fund (FWF): [M 2467-N36] and Nationalstiftung für Forschung, Technologie und Entwicklung, Austria; Ministry of Communications and High Technologies, National Nuclear Research Center, Azerbaijan; Conselho Nacional de Desenvolvimento Científico e Tecnológico (CNPq), Financiadora de Estudos e Projetos (Finep), Fundação de Amparo à Pesquisa do Estado de São Paulo (FAPESP) and Universidade Federal do Rio Grande do Sul (UFRGS), Brazil; Bulgarian Ministry of Education and Science, within the National Roadmap for Research Infrastructures 2020-2027 (object CERN), Bulgaria; Ministry of Education of China (MOEC), Ministry of Science & Technology of China (MSTC) and National Natural Science Foundation of China (NSFC), China; Ministry of Science and Education and Croatian Science Foundation, Croatia; Centro de Aplicaciones Tecnológicas y Desarrollo Nuclear (CEADEN), Cubaenergía, Cuba; Ministry of Education, Youth and Sports of the Czech Republic, Czech Republic; The Danish Council for Independent Research | Natural Sciences, the VILLUM FONDEN and Danish National Research Foundation (DNRF), Denmark; Helsinki Institute of Physics (HIP), Finland; Commissariat à l’Energie Atomique (CEA) and Institut National de Physique Nucléaire et de Physique des Particules (IN2P3) and Centre National de la Recherche Scientifique (CNRS), France; Bundesministerium für Bildung und Forschung (BMBF) and GSI Helmholtzzentrum für Schwerionenforschung GmbH, Germany; General Secretariat for Research and Technology, Ministry of Education, Research and Religions, Greece; National Research, Development and Innovation Office, Hungary; Department of Atomic Energy Government of India (DAE), Department of Science and Technology, Government of India (DST), University Grants Commission, Government of India (UGC) and Council of Scientific and Industrial Research (CSIR), India; National Research and Innovation Agency - BRIN, Indonesia; Istituto Nazionale di Fisica Nucleare (INFN), Italy; Japanese Ministry of Education, Culture, Sports, Science and Technology (MEXT) and Japan Society for the Promotion of Science (JSPS) KAKENHI, Japan; Consejo Nacional de Ciencia (CONACYT) y Tecnología, through Fondo de Cooperación Internacional en Ciencia y Tecnología (FONCICYT) and Dirección General de Asuntos del Personal Académico (DGAPA), Mexico; Nederlandse Organisatie voor Wetenschappelijk Onderzoek (NWO), Netherlands; The Research Council of Norway, Norway; Pontificia Universidad Católica del Perú, Peru; Ministry of Science and Higher Education, National Science Centre and WUT ID-UB, Poland; Korea Institute of Science and Technology Information and National Research Foundation of Korea (NRF), Republic of Korea; Ministry of Education and Scientific Research, Institute of Atomic Physics, Ministry of Research and Innovation and Institute of Atomic Physics and Universitatea Nationala de Stiinta si Tehnologie Politehnica Bucuresti, Romania; Ministry of Education, Science, Research and Sport of the Slovak Republic, Slovakia; National Research Foundation of South Africa, South Africa; Swedish Research Council (VR) and Knut & Alice Wallenberg Foundation (KAW), Sweden; European Organization for Nuclear Research, Switzerland; Suranaree University of Technology (SUT), National Science and Technology Development Agency (NSTDA) and National Science, Research and Innovation Fund (NSRF via PMU-B B05F650021), Thailand; Turkish Energy, Nuclear and Mineral Research Agency (TENMAK), Turkey; National Academy of Sciences of Ukraine, Ukraine; Science and Technology Facilities Council (STFC), United Kingdom; National Science Foundation of the United States of America (NSF) and United States Department of Energy, Office of Nuclear Physics (DOE NP), United States of America. In addition, individual groups or members have received support from: Czech Science Foundation (grant no. 23-07499S), Czech Republic; FORTE project, reg.

no. CZ.02.01.01/00/22_008/0004632, Czech Republic, co-funded by the European Union, Czech Republic; European Research Council (grant no. 950692), European Union; ICSC - Centro Nazionale di Ricerca in High Performance Computing, Big Data and Quantum Computing, European Union - NextGenerationEU; Academy of Finland (Center of Excellence in Quark Matter) (grant nos. 346327, 346328), Finland.

References

- [1] **ALICE** Collaboration, S. Acharya *et al.*, “Measurement of the inclusive isolated-photon production cross section in pp and Pb-Pb collisions at $\sqrt{s_{NN}} = 5.02$ TeV.” CERN-EP-2024-244, 2024. <https://cds.cern.ch/record/2910209>.
- [2] **ALICE** Collaboration, S. Acharya *et al.*, “Performance of the ALICE Electromagnetic Calorimeter”, *JINST* **18** (2023) P08007, arXiv:2209.04216 [physics.ins-det].
- [3] **ALICE** Collaboration, S. Acharya *et al.*, “Measurement of the inclusive isolated photon production cross section in pp collisions at $\sqrt{s} = 7$ TeV”, *Eur. Phys. J. C* **79** (2019) 896, arXiv:1906.01371 [nucl-ex].
- [4] **ALICE** Collaboration, S. Acharya *et al.*, “Measurement of the inclusive isolated-photon production cross section in pp collisions at $\sqrt{s} = 13$ TeV”, arXiv:2407.01165 [hep-ex].
- [5] **ALICE** Collaboration, S. Acharya *et al.*, “Measurement of isolated photon-hadron correlations in $\sqrt{s_{NN}} = 5.02$ TeV pp and p–Pb collisions”, *Phys. Rev. C* **102** (2020) 044908, arXiv:2005.14637 [nucl-ex].
- [6] **ALICE EMCAL** Collaboration, U. Abeysekara *et al.*, “ALICE EMCAL Physics Performance Report”, arXiv:1008.0413 [physics.ins-det].
- [7] M. Cacciari, G. P. Salam, and S. Sapeta, “On the characterisation of the underlying event”, *JHEP* **2010** (2010) 65, arXiv:0912.4926 [hep-ph].
- [8] T. Sjöstrand *et al.*, “An Introduction to PYTHIA 8.2”, *Comput. Phys. Commun.* **191** (2015) 159–177, arXiv:1410.3012 [hep-ph].
- [9] P. Skands, S. Carrazza, and J. Rojo, “Tuning PYTHIA 8.1: the Monash 2013 tune”, *Eur. Phys. J. C* **74** (2014) 3024, arXiv:1404.5630 [hep-ph].
- [10] C. Bierlich, *et al.*, “Codebase release 8.3 for PYTHIA”, *SciPost Phys. Codebases* (2022) 8–r8.3. <https://scipost.org/10.21468/SciPostPhysCodeb.8-r8.3>.
- [11] **ALICE** Collaboration, J. Adam *et al.*, “Anisotropic flow of charged particles in Pb-Pb collisions at $\sqrt{s_{NN}} = 5.02$ TeV”, *Phys. Rev. Lett.* **116** (2016) 132302, arXiv:1602.01119 [nucl-ex].
- [12] C. Loizides and A. Morsch, “Absence of jet quenching in peripheral nucleus–nucleus collisions”, *Phys. Lett. B* **773** (2017) 408–411, arXiv:1705.08856 [nucl-ex].
- [13] S. Catani, M. Fontannaz, J. Guillet, and E. Pilon, “Cross-section of isolated prompt photons in hadron hadron collisions”, *JHEP* **0205** (2002) 028, arXiv:hep-ph/0204023 [hep-ph].
- [14] P. Aurenche, M. Fontannaz, J.-P. Guillet, E. Pilon, and M. Werlen, “A new critical study of photon production in hadronic collisions”, *Phys. Rev. D* **73** (2006) 094007, arXiv:hep-ph/0602133 [hep-ph].
- [15] L. Bourhis, M. Fontannaz, and J. Guillet, “Quarks and gluon fragmentation functions into photons”, *Eur. Phys. J. C* **2** (1998) 529–537, arXiv:hep-ph/9704447 [hep-ph].






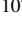






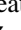


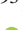
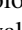
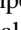
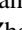
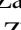


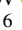






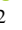
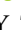







- [16] R. A. Khalek, R. Gauld, T. Giani, E. R. Nocera, T. R. Rabemananjara, and J. Rojo, “nNNPDF3.0: Evidence for a modified partonic structure in heavy nuclei”, *Eur. Phys. J. C* **82** (2022) 507, arXiv:2201.12363 [hep-ph].
- [17] **ALICE** Collaboration, S. Acharya *et al.*, “Centrality determination in heavy-ion collisions”, 2018. <https://cds.cern.ch/record/2636623>. ALICE-PUBLIC-2018-011.
- [18] **CMS** Collaboration, A. M. Sirunyan *et al.*, “The production of isolated photons in PbPb and pp collisions at $\sqrt{s_{\text{NN}}} = 5.02$ TeV”, *JHEP* **07** (2020) 116, arXiv:2003.12797 [hep-ex].
- [19] C. Loizides, J. Kamin, and D. d’Enterria, “Erratum: Improved Monte Carlo Glauber predictions at present and future nuclear colliders [Phys. Rev. C 97, 054910 (2018)]”, *Phys. Rev. C* **99** (2019) 019901.
- [20] **CMS** Collaboration, A. M. Sirunyan *et al.*, “Constraints on the Initial State of Pb–Pb Collisions via Measurements of Z-Boson Yields and Azimuthal Anisotropy at $\sqrt{s_{\text{NN}}} = 5.02$ TeV”, *Phys. Rev. Lett.* **127** (2021) 102002, arXiv:2103.14089 [hep-ex].

A The ALICE Collaboration

S. Acharya¹²⁶, A. Agarwal¹³⁴, G. Aglieri Rinella³², L. Aglietta²⁴, M. Agnello²⁹, N. Agrawal²⁵, Z. Ahammed¹³⁴, S. Ahmad¹⁵, S.U. Ahn⁷¹, I. Ahuja³⁷, A. Akindinov¹⁴⁰, V. Akishina³⁸, M. Al-Turany⁹⁶, D. Aleksandrov¹⁴⁰, B. Alessandro⁵⁶, H.M. Alfanda⁶, R. Alfaro Molina⁶⁷, B. Ali¹⁵, A. Alici²⁵, N. Alizadehvandchali¹¹⁵, A. Alkin¹⁰³, J. Alme²⁰, G. Alocco^{24,52}, T. Alt⁶⁴, A.R. Altamura⁵⁰, I. Altsybeev⁹⁴, J.R. Alvarado⁴⁴, C.O.R. Alvarez⁴⁴, M.N. Anaam⁶, C. Andrei⁴⁵, N. Andreou¹¹⁴, A. Andronic¹²⁵, E. Andronov¹⁴⁰, V. Anguelov⁹³, F. Antinori⁵⁴, P. Antonioli⁵¹, N. Apadula⁷³, L. Aphecetche¹⁰², H. Appelshäuser⁶⁴, C. Arata⁷², S. Arcelli²⁵, R. Arnaldi⁵⁶, J.G.M.C.A. Arneiro¹⁰⁹, I.C. Arsene¹⁹, M. Arslandok¹³⁷, A. Augustinus³², R. Averbeck⁹⁶, D. Averyanov¹⁴⁰, M.D. Azmi¹⁵, H. Baba¹²³, A. Badalà⁵³, J. Bae¹⁰³, Y. Bae¹⁰³, Y.W. Baek⁴⁰, X. Bai¹¹⁹, R. Bailhache⁶⁴, Y. Bailung⁴⁸, R. Bala⁹⁰, A. Balbino²⁹, A. Baldisseri¹²⁹, B. Balis², Z. Banoo⁹⁰, V. Barbasova³⁷, F. Barile³¹, L. Barioglio⁵⁶, M. Barlou⁷⁷, B. Barman⁴¹, G.G. Barnaföldi⁴⁶, L.S. Barnby¹¹⁴, E. Barreau¹⁰², V. Barret¹²⁶, L. Barreto¹⁰⁹, C. Bartels¹¹⁸, K. Barth³², E. Bartsch⁶⁴, N. Bastid¹²⁶, S. Basu⁷⁴, G. Batigne¹⁰², D. Battistini⁹⁴, B. Batyunya¹⁴¹, D. Bauri⁴⁷, J.L. Bazo Alba¹⁰⁰, I.G. Bearden⁸², C. Beattie¹³⁷, P. Becht⁹⁶, D. Behera⁴⁸, I. Belikov¹²⁸, A.D.C. Bell Hechavarria¹²⁵, F. Bellini²⁵, R. Bellwied¹¹⁵, S. Belokurova¹⁴⁰, L.G.E. Beltran¹⁰⁸, Y.A.V. Beltran⁴⁴, G. Bencedi⁴⁶, A. Bensaoula¹¹⁵, S. Beole²⁴, Y. Berdnikov¹⁴⁰, A. Berdnikova⁹³, L. Bergmann⁹³, M.G. Besoiu⁶³, L. Betev³², P.P. Bhaduri¹³⁴, A. Bhasin⁹⁰, B. Bhattacharjee⁴¹, L. Bianchi²⁴, J. Bielčík³⁵, J. Bielčíková⁸⁵, A.P. Bigot¹²⁸, A. Bilandzic⁹⁴, G. Biro⁴⁶, S. Biswas⁴, N. Bize¹⁰², J.T. Blair¹⁰⁷, D. Blau¹⁴⁰, M.B. Blidaru⁹⁶, N. Bluhme³⁸, C. Blume⁶⁴, F. Bock⁸⁶, T. Bodova²⁰, J. Bok¹⁶, L. Boldizsár⁴⁶, M. Bombara³⁷, P.M. Bond³², G. Bonomi^{133,55}, H. Borel¹²⁹, A. Borissov¹⁴⁰, A.G. Borquez Carcamo⁹³, E. Botta²⁴, Y.E.M. Bouziani⁶⁴, L. Bratrud⁶⁴, P. Braun-Munzinger⁹⁶, M. Bregant¹⁰⁹, M. Broz³⁵, G.E. Bruno^{95,31}, V.D. Buchakchiev³⁶, M.D. Buckland⁸⁴, D. Budnikov¹⁴⁰, H. Buesching⁶⁴, S. Bufalino²⁹, P. Buhler¹⁰¹, N. Burmasov¹⁴⁰, Z. Buthelezi^{68,122}, A. Bylinkin²⁰, S.A. Bysiak¹⁰⁶, J.C. Cabanillas Noris¹⁰⁸, M.F.T. Cabrera¹¹⁵, H. Caines¹³⁷, A. Caliva²⁸, E. Calvo Villar¹⁰⁰, J.M.M. Camacho¹⁰⁸, P. Camerini²³, F.D.M. Canedo¹⁰⁹, S.L. Cantway¹³⁷, M. Carabas¹¹², A.A. Carballo³², F. Carnesecchi³², R. Caron¹²⁷, L.A.D. Carvalho¹⁰⁹, J. Castillo Castellanos¹²⁹, M. Castoldi³², F. Catalano³², S. Cattaruzzi²³, R. Cerri²⁴, I. Chakaberia⁷³, P. Chakraborty¹³⁵, S. Chandra¹³⁴, S. Chapeland³², M. Chartier¹¹⁸, S. Chattopadhyay¹³⁴, M. Chen³⁹, T. Cheng⁶, C. Cheshkov¹²⁷, D. Chiappara²⁷, V. Chibante Barroso³², D.D. Chinellato¹⁰¹, E.S. Chizzali^{11,94}, J. Cho⁵⁸, S. Cho⁵⁸, P. Chochula³², Z.A. Chochulska¹³⁵, D. Choudhury⁴¹, S. Choudhury⁹⁸, P. Christakoglou⁸³, C.H. Christensen⁸², P. Christiansen⁷⁴, T. Chujo¹²⁴, M. Ciaccio²⁹, C. Cicalo⁵², F. Cindolo⁵¹, M.R. Ciupek⁹⁶, G. Clai^{111,51}, F. Colamaria⁵⁰, J.S. Colburn⁹⁹, D. Colella³¹, A. Colelli³¹, M. Colocci²⁵, M. Concas³², G. Conesa Balbastre⁷², Z. Conesa del Valle¹³⁰, G. Contin²³, J.G. Contreras³⁵, M.L. Coquet¹⁰², P. Cortese^{132,56}, M.R. Cosentino¹¹¹, F. Costa³², S. Costanza^{21,55}, C. Cot¹³⁰, P. Crochet¹²⁶, M.M. Czarnynoga¹³⁵, A. Dainese⁵⁴, G. Dange³⁸, M.C. Danisch⁹³, A. Danu⁶³, P. Das^{32,79}, S. Das⁴, A.R. Dash¹²⁵, S. Dash⁴⁷, A. De Caro²⁸, G. de Cataldo⁵⁰, J. de Cuveland³⁸, A. De Falco²², D. De Gruttola²⁸, N. De Marco⁵⁶, C. De Martin²³, S. De Pasquale²⁸, R. Deb¹³³, R. Del Grande⁹⁴, L. Dello Stritto³², W. Deng⁶, K.C. Devereaux¹⁸, P. Dhankher¹⁸, D. Di Bari³¹, A. Di Mauro³², B. Di Ruzza¹³¹, B. Diab¹²⁹, R.A. Diaz^{141,7}, Y. Ding⁶, J. Ditzel⁶⁴, R. Divià³², Ø. Djuvsland²⁰, U. Dmitrieva¹⁴⁰, A. Dobrin⁶³, B. Dönigus⁶⁴, J.M. Dubinski¹³⁵, A. Dubla⁹⁶, P. Dupieux¹²⁶, N. Dzalaiova¹³, T.M. Eder¹²⁵, R.J. Ehlers⁷³, F. Eisenhut⁶⁴, R. Ejima⁹¹, D. Elia⁵⁰, B. Erazmus¹⁰², F. Ercolessi²⁵, B. Espagnon¹³⁰, G. Eulisse³², D. Evans⁹⁹, S. Evdokimov¹⁴⁰, L. Fabbietti⁹⁴, M. Faggin²³, J. Faivre⁷², F. Fan⁶, W. Fan⁷³, A. Fantoni⁴⁹, M. Fasel⁸⁶, G. Feofilov¹⁴⁰, A. Fernández Téllez⁴⁴, L. Ferrandi¹⁰⁹, M.B. Ferrer³², A. Ferrero¹²⁹, C. Ferrero^{IV,56}, A. Ferretti²⁴, V.J.G. Feuillard⁹³, V. Filova³⁵, D. Finogeev¹⁴⁰, F.M. Fionda⁵², E. Flatland³², F. Flor^{137,115}, A.N. Flores¹⁰⁷, S. Foertsch⁶⁸, I. Fokin⁹³, S. Fokin¹⁴⁰, U. Follo^{IV,56}, E. Fragiaco⁵⁷, E. Frajna⁴⁶, U. Fuchs³², N. Funicello²⁸, C. Furget⁷², A. Furs¹⁴⁰, T. Fusayasu⁹⁷, J.J. Gaardhøje⁸², M. Gagliardi²⁴, A.M. Gago¹⁰⁰, T. Gahlaut⁴⁷, C.D. Galvan¹⁰⁸, S. Gami⁷⁹, D.R. Gangadharan¹¹⁵, P. Ganoti⁷⁷, C. Garabatos⁹⁶, J.M. Garcia⁴⁴, T. García Chávez⁴⁴, E. Garcia-Solis⁹, C. Gargiulo³², P. Gasik⁹⁶, H.M. Gaur³⁸, A. Gautam¹¹⁷, M.B. Gay Ducati⁶⁶, M. Germain¹⁰², R.A. Gernhaeuser⁹⁴, C. Ghosh¹³⁴, M. Giacalone⁵¹, G. Gioachin²⁹, S.K. Giri¹³⁴, P. Giubellino^{96,56}, P. Giubilato²⁷, A.M.C. Glaenger¹²⁹, P. Glässel⁹³, E. Glimos¹²¹, D.J.Q. Goh⁷⁵, V. Gonzalez¹³⁶, P. Gordeev¹⁴⁰, M. Gorgon², K. Goswami⁴⁸, S. Gotovac³³, V. Grabski⁶⁷, L.K. Graczykowski¹³⁵, E. Grecka⁸⁵, A. Grelli⁵⁹, C. Grigoras³², V. Grigoriev¹⁴⁰, S. Grigoryan^{141,1},

F. Groša ³², J.F. Grosse-Oetringhaus ³², R. Grosso ⁹⁶, D. Grund ³⁵, N.A. Grunwald ⁹³,
 G.G. Guardiano ¹¹⁰, R. Guernane ⁷², M. Guilbaud ¹⁰², K. Gulbrandsen ⁸², J.J.W.K. Gumprecht ¹⁰¹,
 T. Gündem ⁶⁴, T. Gunji ¹²³, W. Guo ⁶, A. Gupta ⁹⁰, R. Gupta ⁹⁰, R. Gupta ⁴⁸, K. Gwizdziel ¹³⁵,
 L. Gyulai ⁴⁶, C. Hadjidakis ¹³⁰, F.U. Haider ⁹⁰, S. Haidlova ³⁵, M. Haldar ⁴, H. Hamagaki ⁷⁵,
 Y. Han ¹³⁹, B.G. Hanley ¹³⁶, R. Hannigan ¹⁰⁷, J. Hansen ⁷⁴, M.R. Haque ⁹⁶, J.W. Harris ¹³⁷,
 A. Harton ⁹, M.V. Hartung ⁶⁴, H. Hassan ¹¹⁶, D. Hatzifotiadou ⁵¹, P. Hauer ⁴², L.B. Havener ¹³⁷,
 E. Hellbär ³², H. Helstrup ³⁴, M. Hemmer ⁶⁴, T. Herman ³⁵, S.G. Hernandez ¹¹⁵, G. Herrera Corral ⁸,
 S. Herrmann ¹²⁷, K.F. Hetland ³⁴, B. Heybeck ⁶⁴, H. Hillemanns ³², B. Hippolyte ¹²⁸, I.P.M. Hobus ⁸³,
 F.W. Hoffmann ⁷⁰, B. Hofman ⁵⁹, M. Horst ⁹⁴, A. Horzyk ², Y. Hou ⁶, P. Hristov ³², P. Huhn ⁶⁴,
 L.M. Huhta ¹¹⁶, T.J. Humanic ⁸⁷, A. Hutson ¹¹⁵, D. Hutter ³⁸, M.C. Hwang ¹⁸, R. Ilkaev ¹⁴⁰,
 M. Inaba ¹²⁴, G.M. Innocenti ³², M. Ippolitov ¹⁴⁰, A. Isakov ⁸³, T. Isidori ¹¹⁷, M.S. Islam ^{47,98},
 S. Iurchenko ¹⁴⁰, M. Ivanov ¹³, M. Ivanov ⁹⁶, V. Ivanov ¹⁴⁰, K.E. Iversen ⁷⁴, M. Jablonski ²,
 B. Jacak ^{18,73}, N. Jacazio ²⁵, P.M. Jacobs ⁷³, S. Jadlovská ¹⁰⁵, J. Jadlovsky ¹⁰⁵, S. Jaelani ⁸¹, C. Jahnke ¹⁰⁹,
 M.J. Jakubowska ¹³⁵, M.A. Janik ¹³⁵, T. Janson ⁷⁰, S. Ji ¹⁶, S. Jia ¹⁰, T. Jiang ¹⁰, A.A.P. Jimenez ⁶⁵,
 F. Jonas ⁷³, D.M. Jones ¹¹⁸, J.M. Jowett ^{32,96}, J. Jung ⁶⁴, M. Jung ⁶⁴, A. Junique ³², A. Jusko ⁹⁹,
 J. Kaewjai ¹⁰⁴, P. Kalinak ⁶⁰, A. Kalweit ³², A. Karasu Uysal ^{V,138}, D. Karatovic ⁸⁸, N. Karatzenis ⁹⁹,
 O. Karavichev ¹⁴⁰, T. Karavicheva ¹⁴⁰, E. Karpechev ¹⁴⁰, M.J. Karwowska ¹³⁵, U. Kebschull ⁷⁰,
 M. Keil ³², B. Ketzer ⁴², J. Keul ⁶⁴, S.S. Khade ⁴⁸, A.M. Khan ¹¹⁹, S. Khan ¹⁵, A. Khanzadeev ¹⁴⁰,
 Y. Kharlov ¹⁴⁰, A. Khatun ¹¹⁷, A. Khuntia ³⁵, Z. Khuranova ⁶⁴, B. Kileng ³⁴, B. Kim ¹⁰³, C. Kim ¹⁶,
 D.J. Kim ¹¹⁶, D. Kim ¹⁰³, E.J. Kim ⁶⁹, J. Kim ¹³⁹, J. Kim ⁵⁸, J. Kim ^{32,69}, M. Kim ¹⁸, S. Kim ¹⁷,
 T. Kim ¹³⁹, K. Kimura ⁹¹, A. Kirkova ³⁶, S. Kirsch ⁶⁴, I. Kisel ³⁸, S. Kiselev ¹⁴⁰, A. Kisiel ¹³⁵,
 J.L. Klay ⁵, J. Klein ³², S. Klein ⁷³, C. Klein-Bösing ¹²⁵, M. Kleiner ⁶⁴, T. Klemenz ⁹⁴, A. Kluge ³²,
 C. Kobdaj ¹⁰⁴, R. Kohara ¹²³, T. Kollegger ⁹⁶, A. Kondratyev ¹⁴¹, N. Kondratyeva ¹⁴⁰, J. König ⁶⁴,
 S.A. Königstorfer ⁹⁴, P.J. Konopka ³², G. Kornakov ¹³⁵, M. Korwieser ⁹⁴, S.D. Koryciak ², C. Koster ⁸³,
 A. Kotliarov ⁸⁵, N. Kovacic ⁸⁸, V. Kovalenko ¹⁴⁰, M. Kowalski ¹⁰⁶, V. Kozhuharov ³⁶, G. Kozlov ³⁸,
 I. Králik ⁶⁰, A. Kravčáková ³⁷, L. Krcal ^{32,38}, M. Krivda ^{99,60}, F. Krizek ⁸⁵, K. Krizkova Gajdosova ³²,
 C. Krug ⁶⁶, M. Krüger ⁶⁴, D.M. Krupova ³⁵, E. Kryshen ¹⁴⁰, V. Kučera ⁵⁸, C. Kuhn ¹²⁸,
 P.G. Kuijer ⁸³, T. Kumaoka ¹²⁴, D. Kumar ¹³⁴, L. Kumar ⁸⁹, N. Kumar ⁸⁹, S. Kumar ⁵⁰, S. Kundu ³²,
 P. Kurashvili ⁷⁸, A.B. Kurepin ¹⁴⁰, A. Kuryakin ¹⁴⁰, S. Kushpil ⁸⁵, V. Kuskov ¹⁴⁰, M. Kutyla ¹³⁵,
 A. Kuznetsov ¹⁴¹, M.J. Kweon ⁵⁸, Y. Kwon ¹³⁹, S.L. La Pointe ³⁸, P. La Rocca ²⁶, A. Lakrathok ¹⁰⁴,
 M. Lamanna ³², A.R. Landou ⁷², R. Langoy ¹²⁰, P. Larionov ³², E. Laudi ³², L. Lautner ⁹⁴,
 R.A.N. Laveaga ¹⁰⁸, R. Lavicka ¹⁰¹, R. Lea ^{133,55}, H. Lee ¹⁰³, I. Legrand ⁴⁵, G. Legras ¹²⁵,
 J. Lehrbach ³⁸, A.M. Lejeune ³⁵, T.M. Lelek ², R.C. Lemmon ^{1,84}, I. León Monzón ¹⁰⁸, M.M. Lesch ⁹⁴,
 E.D. Lesser ¹⁸, P. Lévai ⁴⁶, M. Li ⁶, P. Li ¹⁰, X. Li ¹⁰, B.E. Liang-gilman ¹⁸, J. Lien ¹²⁰, R. Lietava ⁹⁹,
 I. Likmeta ¹¹⁵, B. Lim ²⁴, S.H. Lim ¹⁶, V. Lindenstruth ³⁸, C. Lippmann ⁹⁶, D. Liskova ¹⁰⁵, D.H. Liu ⁶,
 J. Liu ¹¹⁸, G.S.S. Liveraro ¹¹⁰, I.M. Lofnes ²⁰, C. Loizides ⁸⁶, S. Lokos ¹⁰⁶, J. Lömker ⁵⁹,
 X. Lopez ¹²⁶, E. López Torres ⁷, C. Lotteau ¹²⁷, P. Lu ^{96,119}, Z. Lu ¹⁰, F.V. Lugo ⁶⁷, J.R. Luhder ¹²⁵,
 G. Luparello ⁵⁷, Y.G. Ma ³⁹, M. Mager ³², A. Maire ¹²⁸, E.M. Majerz ², M.V. Makariev ³⁶,
 M. Malaev ¹⁴⁰, G. Malfattore ²⁵, N.M. Malik ⁹⁰, S.K. Malik ⁹⁰, D. Mallick ¹³⁰, N. Mallick ^{116,48},
 G. Mandaglio ^{30,53}, S.K. Mandal ⁷⁸, A. Manea ⁶³, V. Manko ¹⁴⁰, F. Manso ¹²⁶, V. Manzari ⁵⁰,
 Y. Mao ⁶, R.W. Marcjan ², G.V. Margagliotti ²³, A. Margotti ⁵¹, A. Marín ⁹⁶, C. Markert ¹⁰⁷,
 C.F.B. Marquez ³¹, P. Martinengo ³², M.I. Martínez ⁴⁴, G. Martínez García ¹⁰², M.P.P. Martins ¹⁰⁹,
 S. Masciocchi ⁹⁶, M. Maserà ²⁴, A. Masoni ⁵², L. Massacrier ¹³⁰, O. Massen ⁵⁹, A. Mastroserio ^{131,50},
 S. Mattiazzi ²⁷, A. Matyja ¹⁰⁶, F. Mazzaschi ^{32,24}, M. Mazzilli ¹¹⁵, Y. Melikyan ⁴³, M. Melo ¹⁰⁹,
 A. Menchaca-Rocha ⁶⁷, J.E.M. Mendez ⁶⁵, E. Meninno ¹⁰¹, A.S. Menon ¹¹⁵, M.W. Menzel ^{32,93},
 M. Meres ¹³, L. Micheletti ³², D. Mihai ¹¹², D.L. Mihaylov ⁹⁴, K. Mikhaylov ^{141,140}, N. Minafra ¹¹⁷,
 D. Miśkowiec ⁹⁶, A. Modak ¹³³, B. Mohanty ⁷⁹, M. Mohisin Khan ^{VI,15}, M.A. Molander ⁴³,
 M.M. Mondal ⁷⁹, S. Monira ¹³⁵, C. Mordasini ¹¹⁶, D.A. Moreira De Godoy ¹²⁵, I. Morozov ¹⁴⁰,
 A. Morsch ³², T. Mrnjavac ³², V. Muccifora ⁴⁹, S. Muhuri ¹³⁴, J.D. Mulligan ⁷³, A. Mulliri ²²,
 M.G. Munhoz ¹⁰⁹, R.H. Munzer ⁶⁴, H. Murakami ¹²³, S. Murray ¹¹³, L. Musa ³², J. Musinsky ⁶⁰,
 J.W. Myrcha ¹³⁵, B. Naik ¹²², A.I. Nambrath ¹⁸, B.K. Nandi ⁴⁷, R. Nania ⁵¹, E. Nappi ⁵⁰,
 A.F. Nassirpour ¹⁷, V. Nastase ¹¹², A. Nath ⁹³, S. Nath ¹³⁴, C. Nattrass ¹²¹, M.N. Naydenov ³⁶, A. Neagu ¹⁹,
 A. Negru ¹¹², E. Nekrasova ¹⁴⁰, L. Nellen ⁶⁵, R. Nepeivoda ⁷⁴, S. Nese ¹⁹, N. Nicassio ⁵⁰, B.S. Nielsen ⁸²,
 E.G. Nielsen ⁸², S. Nikolaev ¹⁴⁰, S. Nikulin ¹⁴⁰, V. Nikulin ¹⁴⁰, F. Noferini ⁵¹, S. Noh ¹²,
 P. Nomokonov ¹⁴¹, J. Norman ¹¹⁸, N. Novitzky ⁸⁶, P. Nowakowski ¹³⁵, A. Nyman ¹⁴⁰, J. Nystrand ²⁰,
 S. Oh ¹⁷, A. Ohlson ⁷⁴, V.A. Okorokov ¹⁴⁰, J. Oleniacz ¹³⁵, A. Onnerstad ¹¹⁶, C. Oppedisano ⁵⁶,

A. Ortiz Velasquez ⁶⁵, J. Otwinowski ¹⁰⁶, M. Oya⁹¹, K. Oyama ⁷⁵, S. Padhan ⁴⁷, D. Pagano ^{133,55}, G. Paić ⁶⁵, S. Paisano-Guzmán ⁴⁴, A. Palasciano ⁵⁰, I. Panasenکو⁷⁴, S. Panebianco ¹²⁹, C. Pantouvakis ²⁷, H. Park ¹²⁴, J. Park ¹²⁴, S. Park ¹⁰³, J.E. Parkkila ³², Y. Patley ⁴⁷, R.N. Patra⁵⁰, B. Paul ¹³⁴, H. Pei ⁶, T. Peitzmann ⁵⁹, X. Peng ¹¹, M. Pennisi ²⁴, S. Perciballi ²⁴, D. Peresunko ¹⁴⁰, G.M. Perez ⁷, Y. Pestov¹⁴⁰, M.T. Petersen⁸², V. Petrov ¹⁴⁰, M. Petrovici ⁴⁵, S. Piano ⁵⁷, M. Pikna ¹³, P. Pillot ¹⁰², O. Pinazza ^{51,32}, L. Pinsky¹¹⁵, C. Pinto ⁹⁴, S. Pisano ⁴⁹, M. Płoskoń ⁷³, M. Planinic⁸⁸, F. Pliquett⁶⁴, D.K. Plociennik ², M.G. Poghosyan ⁸⁶, B. Polichtchouk ¹⁴⁰, S. Politano ²⁹, N. Poljak ⁸⁸, A. Pop ⁴⁵, S. Porteboeuf-Houssais ¹²⁶, V. Pozdniakov ^{1,141}, I.Y. Pozos ⁴⁴, K.K. Pradhan ⁴⁸, S.K. Prasad ⁴, S. Prasad ⁴⁸, R. Preghenella ⁵¹, F. Prino ⁵⁶, C.A. Pruneau ¹³⁶, I. Pshenichnov ¹⁴⁰, M. Puccio ³², S. Pucillo ²⁴, S. Qiu ⁸³, L. Quaglia ²⁴, A.M.K. Radhakrishnan⁴⁸, S. Ragoni ¹⁴, A. Rai ¹³⁷, A. Rakotozafindrabe ¹²⁹, L. Ramello ^{132,56}, M. Rasa ²⁶, S.S. Räsänen ⁴³, R. Rath ⁵¹, M.P. Rauch ²⁰, I. Ravasenga ³², K.F. Read ^{86,121}, C. Reckziegel ¹¹¹, A.R. Redelbach ³⁸, K. Redlich ^{77,78}, C.A. Reetz ⁹⁶, H.D. Regules-Medel⁴⁴, A. Rehman²⁰, F. Reidt ³², H.A. Reme-Ness ³⁴, K. Reygers ⁹³, A. Riabov ¹⁴⁰, V. Riabov ¹⁴⁰, R. Ricci ²⁸, M. Richter ²⁰, A.A. Riedel ⁹⁴, W. Riegler ³², A.G. Riffero ²⁴, M. Rignanese ²⁷, C. Ripoli²⁸, C. Ristea ⁶³, M.V. Rodriguez ³², M. Rodríguez Cahuantzi ⁴⁴, S.A. Rodríguez Ramírez ⁴⁴, K. Røed ¹⁹, R. Rogalev ¹⁴⁰, E. Rogochaya ¹⁴¹, T.S. Rogoschinski ⁶⁴, D. Rohr ³², D. Röhrich ²⁰, S. Rojas Torres ³⁵, P.S. Rokita ¹³⁵, G. Romanenko ²⁵, F. Ronchetti ³², E.D. Rosas⁶⁵, K. Roslon ¹³⁵, A. Rossi ⁵⁴, A. Roy ⁴⁸, S. Roy ⁴⁷, N. Rubini ^{51,25}, J.A. Rudolph⁸³, D. Ruggiano ¹³⁵, R. Rui ²³, P.G. Russek ², R. Russo ⁸³, A. Rustamov ⁸⁰, E. Ryabinkin ¹⁴⁰, Y. Ryabov ¹⁴⁰, A. Rybicki ¹⁰⁶, J. Ryu ¹⁶, W. Rzesza ¹³⁵, B. Sabiu⁵¹, S. Sadovsky ¹⁴⁰, J. Saetre ²⁰, S. Saha ⁷⁹, B. Sahoo ⁴⁸, R. Sahoo ⁴⁸, S. Sahoo⁶¹, D. Sahu ⁴⁸, P.K. Sahu ⁶¹, J. Saini ¹³⁴, K. Sajdakova³⁷, S. Sakai ¹²⁴, M.P. Salvan ⁹⁶, S. Sambyal ⁹⁰, D. Samitz ¹⁰¹, I. Sanna ^{32,94}, T.B. Saramela¹⁰⁹, D. Sarkar ⁸², P. Sarma ⁴¹, V. Sarritzu ²², V.M. Sarti ⁹⁴, M.H.P. Sas ³², S. Sawan ⁷⁹, E. Scapparone ⁵¹, J. Schambach ⁸⁶, H.S. Scheid ⁶⁴, C. Schiaua ⁴⁵, R. Schicker ⁹³, F. Schlepfer ⁹³, A. Schmah⁹⁶, C. Schmidt ⁹⁶, M.O. Schmidt ³², M. Schmidt⁹², N.V. Schmidt ⁸⁶, A.R. Schmier ¹²¹, R. Schotter ^{101,128}, A. Schröter ³⁸, J. Schukraft ³², K. Schweda ⁹⁶, G. Scioli ²⁵, E. Scomparin ⁵⁶, J.E. Seger ¹⁴, Y. Sekiguchi¹²³, D. Sekihata ¹²³, M. Selina ⁸³, I. Selyuzhenkov ⁹⁶, S. Senyukov ¹²⁸, J.J. Seo ⁹³, D. Serebryakov ¹⁴⁰, L. Serkin ⁶⁵, L. Šerkšnytė ⁹⁴, A. Sevcenco ⁶³, T.J. Shaba ⁶⁸, A. Shabetai ¹⁰², R. Shahoyan³², A. Shangaraev ¹⁴⁰, B. Sharma ⁹⁰, D. Sharma ⁴⁷, H. Sharma ⁵⁴, M. Sharma ⁹⁰, S. Sharma ⁷⁵, S. Sharma ⁹⁰, U. Sharma ⁹⁰, A. Shatat ¹³⁰, O. Sheibani^{136,115}, K. Shigaki ⁹¹, M. Shimomura⁷⁶, J. Shin¹², S. Shirinkin ¹⁴⁰, Q. Shou ³⁹, Y. Sibiriak ¹⁴⁰, S. Siddhanta ⁵², T. Siemiarczuk ⁷⁸, T.F. Silva ¹⁰⁹, D. Silvermyr ⁷⁴, T. Simantathammakul¹⁰⁴, R. Simeonov ³⁶, B. Singh⁹⁰, B. Singh ⁹⁴, K. Singh ⁴⁸, R. Singh ⁷⁹, R. Singh ⁹⁰, R. Singh ^{54,96}, S. Singh ¹⁵, V.K. Singh ¹³⁴, V. Singhal ¹³⁴, T. Sinha ⁹⁸, B. Sitar ¹³, M. Sitta ^{132,56}, T.B. Skaali¹⁹, G. Skorodumovs ⁹³, N. Smirnov ¹³⁷, R.J.M. Snellings ⁵⁹, E.H. Solheim ¹⁹, C. Sonnabend ^{32,96}, J.M. Sonneveld ⁸³, F. Soramel ²⁷, A.B. Soto-hernandez ⁸⁷, R. Spijkers ⁸³, I. Sputowska ¹⁰⁶, J. Staa ⁷⁴, J. Stachel ⁹³, I. Stan ⁶³, P.J. Steffanic ¹²¹, T. Stellhorn¹²⁵, S.F. Stiefelmaier ⁹³, D. Stocco ¹⁰², I. Storehaug ¹⁹, N.J. Strangmann ⁶⁴, P. Stratmann ¹²⁵, S. Strazzi ²⁵, A. Sturniolo ^{30,53}, C.P. Stylianidis⁸³, A.A.P. Suaide ¹⁰⁹, C. Suire ¹³⁰, A. Suiu^{32,112}, M. Sukhanov ¹⁴⁰, M. Suljic ³², R. Sultanov ¹⁴⁰, V. Sumberia ⁹⁰, S. Sumowidagdo ⁸¹, M. Szymkowski ¹³⁵, L.H. Tabares⁷, S.F. Taghavi ⁹⁴, J. Takahashi ¹¹⁰, G.J. Tambave ⁷⁹, S. Tang ⁶, Z. Tang ¹¹⁹, J.D. Tapia Takaki ¹¹⁷, N. Tapus¹¹², L.A. Tarasovicova ³⁷, M.G. Tarzila ⁴⁵, A. Tauro ³², A. Tavira García ¹³⁰, G. Tejeda Muñoz ⁴⁴, L. Terlizzi ²⁴, C. Terrevoli ⁵⁰, S. Thakur ⁴, M. Thogersen¹⁹, D. Thomas ¹⁰⁷, A. Tikhonov ¹⁴⁰, N. Tiltmann ^{32,125}, A.R. Timmins ¹¹⁵, M. Tkacik¹⁰⁵, T. Tkacik ¹⁰⁵, A. Toia ⁶⁴, R. Tokumoto⁹¹, S. Tomassini²⁵, K. Tomohiro⁹¹, N. Topilskaya ¹⁴⁰, M. Toppi ⁴⁹, V.V. Torres ¹⁰², A.G. Torres Ramos ³¹, A. Trifiró ^{30,53}, T. Triloki⁹⁵, A.S. Triolo ^{32,30,53}, S. Tripathy ³², T. Tripathy ⁴⁷, S. Trogolo ²⁴, V. Trubnikov ³, W.H. Trzaska ¹¹⁶, T.P. Trzcinski ¹³⁵, C. Tsolanta¹⁹, R. Tu³⁹, A. Tumkin ¹⁴⁰, R. Turrisi ⁵⁴, T.S. Tveter ¹⁹, K. Ullaland ²⁰, B. Ulukutlu ⁹⁴, S. Upadhyaya ¹⁰⁶, A. Uras ¹²⁷, G.L. Usai ²², M. Vala³⁷, N. Valle ⁵⁵, L.V.R. van Doremalen⁵⁹, M. van Leeuwen ⁸³, C.A. van Veen ⁹³, R.J.G. van Weelden ⁸³, P. Vande Vyvre ³², D. Varga ⁴⁶, Z. Varga ^{137,46}, P. Vargas Torres⁶⁵, M. Vasileiou ⁷⁷, A. Vasiliev ^{1,140}, O. Vázquez Doce ⁴⁹, O. Vazquez Rueda ¹¹⁵, V. Vechernin ¹⁴⁰, E. Vercellin ²⁴, R. Verma ⁴⁷, R. Vértesi ⁴⁶, M. Verweij ⁵⁹, L. Vickovic³³, Z. Vilakazi¹²², O. Villalobos Baillie ⁹⁹, A. Villani ²³, A. Vinogradov ¹⁴⁰, T. Virgili ²⁸, M.M.O. Virta ¹¹⁶, A. Vodopyanov ¹⁴¹, B. Volkel ³², M.A. Völkl ⁹³, S.A. Voloshin ¹³⁶, G. Volpe ³¹, B. von Haller ³², I. Vorobyev ³², N. Vozniuk ¹⁴⁰, J. Vrláková ³⁷, J. Wan³⁹, C. Wang ³⁹, D. Wang³⁹, Y. Wang ³⁹, Y. Wang ⁶, Z. Wang ³⁹, A. Wegrzynek ³², F.T. Weiglhofer³⁸, S.C. Wenzel ³², J.P. Wessels ¹²⁵, P. Wiacek ², J. Wiechula ⁶⁴, J. Wikne ¹⁹,

G. Wilk ⁷⁸, J. Wilkinson ⁹⁶, G.A. Willems ¹²⁵, B. Windelband ⁹³, M. Winn ¹²⁹, J.R. Wright ¹⁰⁷, W. Wu³⁹, Y. Wu ¹¹⁹, Z. Xiong¹¹⁹, R. Xu ⁶, A. Yadav ⁴², A.K. Yadav ¹³⁴, Y. Yamaguchi ⁹¹, S. Yang²⁰, S. Yano ⁹¹, E.R. Yeats¹⁸, Z. Yin ⁶, I.-K. Yoo ¹⁶, J.H. Yoon ⁵⁸, H. Yu¹², S. Yuan²⁰, A. Yuncu ⁹³, V. Zaccolo ²³, C. Zampolli ³², F. Zanone ⁹³, N. Zardoshti ³², A. Zarochentsev ¹⁴⁰, P. Závada ⁶², N. Zaviyalov¹⁴⁰, M. Zhalov ¹⁴⁰, B. Zhang ^{93,6}, C. Zhang ¹²⁹, L. Zhang ³⁹, M. Zhang ^{126,6}, M. Zhang ⁶, S. Zhang ³⁹, X. Zhang ⁶, Y. Zhang¹¹⁹, Z. Zhang ⁶, M. Zhao ¹⁰, V. Zhrebchevskii ¹⁴⁰, Y. Zhi¹⁰, D. Zhou ⁶, Y. Zhou ⁸², J. Zhu ^{54,6}, S. Zhu¹¹⁹, Y. Zhu⁶, S.C. Zugravel ⁵⁶, N. Zurlo ^{133,55}

Affiliation Notes

^I Deceased

^{II} Also at: Max-Planck-Institut für Physik, Munich, Germany

^{III} Also at: Italian National Agency for New Technologies, Energy and Sustainable Economic Development (ENEA), Bologna, Italy

^{IV} Also at: Dipartimento DET del Politecnico di Torino, Turin, Italy

^V Also at: Yildiz Technical University, Istanbul, Türkiye

^{VI} Also at: Department of Applied Physics, Aligarh Muslim University, Aligarh, India

^{VII} Also at: Institute of Theoretical Physics, University of Wrocław, Poland

^{VIII} Also at: An institution covered by a cooperation agreement with CERN

Collaboration Institutes

¹ A.I. Alikhanyan National Science Laboratory (Yerevan Physics Institute) Foundation, Yerevan, Armenia

² AGH University of Krakow, Cracow, Poland

³ Bogolyubov Institute for Theoretical Physics, National Academy of Sciences of Ukraine, Kiev, Ukraine

⁴ Bose Institute, Department of Physics and Centre for Astroparticle Physics and Space Science (CAPSS), Kolkata, India

⁵ California Polytechnic State University, San Luis Obispo, California, United States

⁶ Central China Normal University, Wuhan, China

⁷ Centro de Aplicaciones Tecnológicas y Desarrollo Nuclear (CEADEN), Havana, Cuba

⁸ Centro de Investigación y de Estudios Avanzados (CINVESTAV), Mexico City and Mérida, Mexico

⁹ Chicago State University, Chicago, Illinois, United States

¹⁰ China Institute of Atomic Energy, Beijing, China

¹¹ China University of Geosciences, Wuhan, China

¹² Chungbuk National University, Cheongju, Republic of Korea

¹³ Comenius University Bratislava, Faculty of Mathematics, Physics and Informatics, Bratislava, Slovak Republic

¹⁴ Creighton University, Omaha, Nebraska, United States

¹⁵ Department of Physics, Aligarh Muslim University, Aligarh, India

¹⁶ Department of Physics, Pusan National University, Pusan, Republic of Korea

¹⁷ Department of Physics, Sejong University, Seoul, Republic of Korea

¹⁸ Department of Physics, University of California, Berkeley, California, United States

¹⁹ Department of Physics, University of Oslo, Oslo, Norway

²⁰ Department of Physics and Technology, University of Bergen, Bergen, Norway

²¹ Dipartimento di Fisica, Università di Pavia, Pavia, Italy

²² Dipartimento di Fisica dell'Università and Sezione INFN, Cagliari, Italy

²³ Dipartimento di Fisica dell'Università and Sezione INFN, Trieste, Italy

²⁴ Dipartimento di Fisica dell'Università and Sezione INFN, Turin, Italy

²⁵ Dipartimento di Fisica e Astronomia dell'Università and Sezione INFN, Bologna, Italy

²⁶ Dipartimento di Fisica e Astronomia dell'Università and Sezione INFN, Catania, Italy

²⁷ Dipartimento di Fisica e Astronomia dell'Università and Sezione INFN, Padova, Italy

²⁸ Dipartimento di Fisica 'E.R. Caianiello' dell'Università and Gruppo Collegato INFN, Salerno, Italy

²⁹ Dipartimento DISAT del Politecnico and Sezione INFN, Turin, Italy

³⁰ Dipartimento di Scienze MIFT, Università di Messina, Messina, Italy

³¹ Dipartimento Interateneo di Fisica 'M. Merlin' and Sezione INFN, Bari, Italy

³² European Organization for Nuclear Research (CERN), Geneva, Switzerland

- ³³ Faculty of Electrical Engineering, Mechanical Engineering and Naval Architecture, University of Split, Split, Croatia
- ³⁴ Faculty of Engineering and Science, Western Norway University of Applied Sciences, Bergen, Norway
- ³⁵ Faculty of Nuclear Sciences and Physical Engineering, Czech Technical University in Prague, Prague, Czech Republic
- ³⁶ Faculty of Physics, Sofia University, Sofia, Bulgaria
- ³⁷ Faculty of Science, P.J. Šafárik University, Košice, Slovak Republic
- ³⁸ Frankfurt Institute for Advanced Studies, Johann Wolfgang Goethe-Universität Frankfurt, Frankfurt, Germany
- ³⁹ Fudan University, Shanghai, China
- ⁴⁰ Gangneung-Wonju National University, Gangneung, Republic of Korea
- ⁴¹ Gauhati University, Department of Physics, Guwahati, India
- ⁴² Helmholtz-Institut für Strahlen- und Kernphysik, Rheinische Friedrich-Wilhelms-Universität Bonn, Bonn, Germany
- ⁴³ Helsinki Institute of Physics (HIP), Helsinki, Finland
- ⁴⁴ High Energy Physics Group, Universidad Autónoma de Puebla, Puebla, Mexico
- ⁴⁵ Horia Hulubei National Institute of Physics and Nuclear Engineering, Bucharest, Romania
- ⁴⁶ HUN-REN Wigner Research Centre for Physics, Budapest, Hungary
- ⁴⁷ Indian Institute of Technology Bombay (IIT), Mumbai, India
- ⁴⁸ Indian Institute of Technology Indore, Indore, India
- ⁴⁹ INFN, Laboratori Nazionali di Frascati, Frascati, Italy
- ⁵⁰ INFN, Sezione di Bari, Bari, Italy
- ⁵¹ INFN, Sezione di Bologna, Bologna, Italy
- ⁵² INFN, Sezione di Cagliari, Cagliari, Italy
- ⁵³ INFN, Sezione di Catania, Catania, Italy
- ⁵⁴ INFN, Sezione di Padova, Padova, Italy
- ⁵⁵ INFN, Sezione di Pavia, Pavia, Italy
- ⁵⁶ INFN, Sezione di Torino, Turin, Italy
- ⁵⁷ INFN, Sezione di Trieste, Trieste, Italy
- ⁵⁸ Inha University, Incheon, Republic of Korea
- ⁵⁹ Institute for Gravitational and Subatomic Physics (GRASP), Utrecht University/Nikhef, Utrecht, Netherlands
- ⁶⁰ Institute of Experimental Physics, Slovak Academy of Sciences, Košice, Slovak Republic
- ⁶¹ Institute of Physics, Homi Bhabha National Institute, Bhubaneswar, India
- ⁶² Institute of Physics of the Czech Academy of Sciences, Prague, Czech Republic
- ⁶³ Institute of Space Science (ISS), Bucharest, Romania
- ⁶⁴ Institut für Kernphysik, Johann Wolfgang Goethe-Universität Frankfurt, Frankfurt, Germany
- ⁶⁵ Instituto de Ciencias Nucleares, Universidad Nacional Autónoma de México, Mexico City, Mexico
- ⁶⁶ Instituto de Física, Universidade Federal do Rio Grande do Sul (UFRGS), Porto Alegre, Brazil
- ⁶⁷ Instituto de Física, Universidad Nacional Autónoma de México, Mexico City, Mexico
- ⁶⁸ iThemba LABS, National Research Foundation, Somerset West, South Africa
- ⁶⁹ Jeonbuk National University, Jeonju, Republic of Korea
- ⁷⁰ Johann-Wolfgang-Goethe Universität Frankfurt Institut für Informatik, Fachbereich Informatik und Mathematik, Frankfurt, Germany
- ⁷¹ Korea Institute of Science and Technology Information, Daejeon, Republic of Korea
- ⁷² Laboratoire de Physique Subatomique et de Cosmologie, Université Grenoble-Alpes, CNRS-IN2P3, Grenoble, France
- ⁷³ Lawrence Berkeley National Laboratory, Berkeley, California, United States
- ⁷⁴ Lund University Department of Physics, Division of Particle Physics, Lund, Sweden
- ⁷⁵ Nagasaki Institute of Applied Science, Nagasaki, Japan
- ⁷⁶ Nara Women's University (NWU), Nara, Japan
- ⁷⁷ National and Kapodistrian University of Athens, School of Science, Department of Physics, Athens, Greece
- ⁷⁸ National Centre for Nuclear Research, Warsaw, Poland
- ⁷⁹ National Institute of Science Education and Research, Homi Bhabha National Institute, Jatni, India
- ⁸⁰ National Nuclear Research Center, Baku, Azerbaijan
- ⁸¹ National Research and Innovation Agency - BRIN, Jakarta, Indonesia
- ⁸² Niels Bohr Institute, University of Copenhagen, Copenhagen, Denmark
- ⁸³ Nikhef, National institute for subatomic physics, Amsterdam, Netherlands

- 84 Nuclear Physics Group, STFC Daresbury Laboratory, Daresbury, United Kingdom
- 85 Nuclear Physics Institute of the Czech Academy of Sciences, Husinec-Řež, Czech Republic
- 86 Oak Ridge National Laboratory, Oak Ridge, Tennessee, United States
- 87 Ohio State University, Columbus, Ohio, United States
- 88 Physics department, Faculty of science, University of Zagreb, Zagreb, Croatia
- 89 Physics Department, Panjab University, Chandigarh, India
- 90 Physics Department, University of Jammu, Jammu, India
- 91 Physics Program and International Institute for Sustainability with Knotted Chiral Meta Matter (SKCM2), Hiroshima University, Hiroshima, Japan
- 92 Physikalisches Institut, Eberhard-Karls-Universität Tübingen, Tübingen, Germany
- 93 Physikalisches Institut, Ruprecht-Karls-Universität Heidelberg, Heidelberg, Germany
- 94 Physik Department, Technische Universität München, Munich, Germany
- 95 Politecnico di Bari and Sezione INFN, Bari, Italy
- 96 Research Division and ExtreMe Matter Institute EMMI, GSI Helmholtzzentrum für Schwerionenforschung GmbH, Darmstadt, Germany
- 97 Saga University, Saga, Japan
- 98 Saha Institute of Nuclear Physics, Homi Bhabha National Institute, Kolkata, India
- 99 School of Physics and Astronomy, University of Birmingham, Birmingham, United Kingdom
- 100 Sección Física, Departamento de Ciencias, Pontificia Universidad Católica del Perú, Lima, Peru
- 101 Stefan Meyer Institut für Subatomare Physik (SMI), Vienna, Austria
- 102 SUBATECH, IMT Atlantique, Nantes Université, CNRS-IN2P3, Nantes, France
- 103 Sungkyunkwan University, Suwon City, Republic of Korea
- 104 Suranaree University of Technology, Nakhon Ratchasima, Thailand
- 105 Technical University of Košice, Košice, Slovak Republic
- 106 The Henryk Niewodniczanski Institute of Nuclear Physics, Polish Academy of Sciences, Cracow, Poland
- 107 The University of Texas at Austin, Austin, Texas, United States
- 108 Universidad Autónoma de Sinaloa, Culiacán, Mexico
- 109 Universidade de São Paulo (USP), São Paulo, Brazil
- 110 Universidade Estadual de Campinas (UNICAMP), Campinas, Brazil
- 111 Universidade Federal do ABC, Santo Andre, Brazil
- 112 Universitatea Nationala de Stiinta si Tehnologie Politehnica Bucuresti, Bucharest, Romania
- 113 University of Cape Town, Cape Town, South Africa
- 114 University of Derby, Derby, United Kingdom
- 115 University of Houston, Houston, Texas, United States
- 116 University of Jyväskylä, Jyväskylä, Finland
- 117 University of Kansas, Lawrence, Kansas, United States
- 118 University of Liverpool, Liverpool, United Kingdom
- 119 University of Science and Technology of China, Hefei, China
- 120 University of South-Eastern Norway, Kongsberg, Norway
- 121 University of Tennessee, Knoxville, Tennessee, United States
- 122 University of the Witwatersrand, Johannesburg, South Africa
- 123 University of Tokyo, Tokyo, Japan
- 124 University of Tsukuba, Tsukuba, Japan
- 125 Universität Münster, Institut für Kernphysik, Münster, Germany
- 126 Université Clermont Auvergne, CNRS/IN2P3, LPC, Clermont-Ferrand, France
- 127 Université de Lyon, CNRS/IN2P3, Institut de Physique des 2 Infinis de Lyon, Lyon, France
- 128 Université de Strasbourg, CNRS, IPHC UMR 7178, F-67000 Strasbourg, France, Strasbourg, France
- 129 Université Paris-Saclay, Centre d'Etudes de Saclay (CEA), IRFU, Département de Physique Nucléaire (DPhN), Saclay, France
- 130 Université Paris-Saclay, CNRS/IN2P3, IJCLab, Orsay, France
- 131 Università degli Studi di Foggia, Foggia, Italy
- 132 Università del Piemonte Orientale, Vercelli, Italy
- 133 Università di Brescia, Brescia, Italy
- 134 Variable Energy Cyclotron Centre, Homi Bhabha National Institute, Kolkata, India
- 135 Warsaw University of Technology, Warsaw, Poland
- 136 Wayne State University, Detroit, Michigan, United States

¹³⁷ Yale University, New Haven, Connecticut, United States

¹³⁸ Yildiz Technical University, Istanbul, Turkey

¹³⁹ Yonsei University, Seoul, Republic of Korea

¹⁴⁰ Affiliated with an institute covered by a cooperation agreement with CERN

¹⁴¹ Affiliated with an international laboratory covered by a cooperation agreement with CERN.